Acta Biomaterialia 143 (2022) 266–281

Contents lists available at ScienceDirect

Acta Biomaterialia

journal homepage: www.elsevier.com/locate/actbio

Full length article

Bilayered extracellular matrix derived scaffolds with anisotropic pore architecture guide tissue organization during osteochondral defect repair

David C. Browe[a,b,c,1], Pedro J. Díaz-Payno[a,b,1], Fiona E. Freeman[a,b], Rossana Schipani[a,b], Ross Burdis[a,b], Daniel P. Ahern[a,e,f], Jessica M. Nulty[a,b], Selcan Guler[a], Lindsey D. Randall[a], Conor T. Buckley[a,b,c,d], Pieter A.J. Brama[g], Daniel J. Kelly[a,b,c,d,*]

[a] Trinity Centre for Biomedical Engineering, Trinity Biomedical Sciences Institute, Trinity College Dublin, 152-160 Pearse Street, Dublin 2, Ireland
[b] Discipline of Mechanical, Manufacturing and Biomedical Engineering, School of Engineering, Trinity College Dublin, Ireland
[c] Advanced Materials and Bioengineering Research Centre (AMBER), Royal College of Surgeons in Ireland, Trinity College Dublin, Ireland
[d] Department of Anatomy and Regenerative Medicine, Royal College of Surgeons in Ireland, Dublin, Ireland
[e] School of Medicine, Trinity College Dublin, Dublin, Ireland
[f] National Spinal Injuries Unit, Department of Trauma & Orthopaedic Surgery, Mater Misericordiae University Hospital, Dublin, Ireland
[g] School of Veterinary Medicine, University College Dublin, Ireland

ARTICLE INFO

Article history:
Received 19 November 2021
Revised 2 March 2022
Accepted 4 March 2022
Available online 9 March 2022

Keywords:
Cartilage repair
Extracellular matrix
Biomaterials
Freeze-drying
Preclinical models
Osteochondral
Tissue engineering

ABSTRACT

While some clinical advances in cartilage repair have occurred, osteochondral (OC) defect repair remains a significant challenge, with current scaffold-based approaches failing to recapitulate the complex, hierarchical structure of native articular cartilage (AC). To address this need, we fabricated bilayered extracellular matrix (ECM)-derived scaffolds with aligned pore architectures. By modifying the freeze-drying kinetics and controlling the direction of heat transfer during freezing, it was possible to produce anisotropic scaffolds with larger pores which supported homogenous cellular infiltration and improved sulfated glycosaminoglycan deposition. Neo-tissue organization *in vitro* could also be controlled by altering scaffold pore architecture, with collagen fibres aligning parallel to the long-axis of the pores within scaffolds containing aligned pore networks. Furthermore, we used *in vitro* and *in vivo* assays to demonstrate that AC and bone ECM derived scaffolds could preferentially direct the differentiation of mesenchymal stromal cells (MSCs) towards either a chondrogenic or osteogenic lineage respectively, enabling the development of bilayered ECM scaffolds capable of spatially supporting unique tissue phenotypes. Finally, we implanted these scaffolds into a large animal model of OC defect repair. After 6 months *in vivo*, scaffold implantation was found to improve cartilage matrix deposition, with collagen fibres preferentially aligning parallel to the long axis of the scaffold pores, resulting in a repair tissue that structurally and compositionally was more hyaline-like in nature. These results demonstrate how scaffold architecture and composition can be spatially modulated to direct the regeneration of complex interfaces such as the osteochondral unit, enabling their use as cell-free, off-the-shelf implants for joint regeneration.

Statement of significance

The architecture of the extracellular matrix, while integral to tissue function, is often neglected in the design and evaluation of regenerative biomaterials. In this study we developed a bilayered scaffold for osteochondral defect repair consisting of tissue-specific extracellular matrix (ECM)-derived biomaterials to spatially direct stem/progenitor cell differentiation, with a tailored pore microarchitecture to promote the development of a repair tissue that recapitulates the hierarchical structure of native AC. The use of

* Corresponding author at: Trinity Centre for Biomedical Engineering, Trinity Biomedical Sciences Institute, Trinity College Dublin, 152-160 Pearse Street, Dublin 2, Ireland.
E-mail address: kellyd9@tcd.ie (D.J. Kelly).
[1] These authors contributed equally to this work.

https://doi.org/10.1016/j.actbio.2022.03.009

this bilayered scaffold resulted in improved tissue repair outcomes in a large animal model, specifically the ability to guide neo-tissue organization and therefore recapitulate key aspects of the zonal structure of native articular cartilage. These bilayer scaffolds have the potential to become a new therapeutic option for osteochondral defect repair.

1. Introduction

The complex composition and structure of articular cartilage (AC), consisting of an arcade-like collagen fibre network and negatively charged proteoglycans, enables it to withstand challenging biomechanical loads and distribute them across the surface of synovial joints [1–4]. In defects where the AC is extensively worn and the subchondral bone is exposed, surgical intervention is required to induce repair and prevent further joint degeneration and the onset of osteoarthritis (OA) [5,6]. While some clinical advances in cartilage repair have occurred, cartilage and osteochondral defect repair remain significant clinical challenges, with current tissue engineering and/or "off-the-shelf" scaffold-based approaches failing to fully recapitulate the complex, hierarchical microarchitecture of native AC [7–11].

The use of osteochondral autograft/allograft transplantation is a viable treatment option for the repair of chondral and osteochondral (OC) defects [12] but it is not without drawbacks. This technique involves the transplantation of an osteochondral plug consisting of viable hyaline cartilage on top of bone from either the patient themselves or a donor. Such treatments allow patients to return to activity faster than other treatments, but are limited by factors such as donor site morbidity for autograft transplantation [12] and the lack of available donors, high cost and risk of disease transmission for allograft transplantation [13]. There are also several biphasic scaffolds for OC defect repair that are, or have previously been, approved for human clinical use; these include TruFit® (Smith and Nephew [14]), Agili-C® (CartiHeal [15,16]), OsseoFit® plug (Kensey Nash Corp [17]) and MaioRegen® (Finceramica [18]). While the composition of these products varies, consisting of various natural and synthetic polymers, minerals, type I collagen and/or hyaluronic acid (HA), none of these products are derived directly from the tissue which they are trying to regenerate. Therefore, they may not preferentially promote true tissue-specific regeneration when they are colonised by endogenous stem/progenitor cells post implantation. Tissue-specific extracellular matrix (ECM) derived scaffolds have been shown to promote tissue repair by providing both structural and functional cues to cells [19–22], suggesting that such natural, biomimetic materials may provide a cell-inductive platform for the regeneration of musculoskeletal tissues. Indeed, decellularized AC-ECM derived scaffolds have been shown to promote the chondrogenic differentiation of mesenchymal stem/stromal cells (MSCs) [22–27], while bone [28–30] and growth plate [24,31] ECM derived scaffolds have been shown to support osteogenesis. However, directing the phenotype of stem/progenitor cells is only the first step in ensuring successful cartilage or OC defect repair following scaffold implantation; such biomaterials are also required to direct the structural organization of the repair tissue to promote functional regeneration.

Recent studies have highlighted the importance of scaffold/biomaterial architecture in directing successful cartilage tissue engineering. For example, cellular and neotissue alignment within decellularized cartilage explants is influenced by the underlying collagen architecture of the decellularized tissue [32]. The architecture of porous scaffolds has also been shown to influence multiple factors such as cell infiltration [33,34], matrix deposition [35], scaffold mechanical properties [36] and the transport of nutrients and waste products into and out of the scaffold [33]. In order to improve tissue deposition, a number of different approaches have been proposed to modify the internal architecture of porous scaffolds. For example, alteration of freeze-drying parameters can be used to obtain biologically active scaffolds with tailorable interconnected pores of defined shape and size [34,37–41]. Whether scaffold pore alignment can be modulated to regulate both cellular infiltration and neo-tissue organization during AC regeneration remains poorly understood.

The overall goal of this study was to develop an 'off-the-shelf', biphasic scaffold for osteochondral defect repair that combines tissue-specific ECM-derived biomaterials to direct AC or bone development with a tailored pore architecture to recapitulate the hierarchical collagen structure of AC. To realise this goal, we first developed a freeze-drying methodology in order to: (i) increase the mean pore size of the AC-ECM scaffolds, and (ii) to create anisotropic scaffolds with an aligned pore orientation. The effect of these alterations on chondrogenic differentiation of MSCs was subsequently examined *in vitro*. To select the optimal ECM material for the osseous layer of the bilayered scaffold, we fabricated and subcutaneously implanted three ECM-derived scaffolds derived from solubilized growth plate (GP) cartilage, AC and bone and evaluated their ability to promote osteogenic differentiation of MSCs *in vivo*. Finally, having determined the optimized bilayer scaffold to preferentially direct OC tissue differentiation *in vitro,* we then assessed the capacity of such bilayered ECM derived scaffolds to regenerate an OC defect in a clinically relevant caprine model of OC defect repair. We hypothesized that this combination of tissue-specific ECM biomaterials with a tailored pore microarchitecture could promote the development of a repair tissue that recapitulates the zonal architecture and composition of the native osteochondral unit, ultimately leading to better regenerative outcomes.

2. Materials and methods

2.1. ECM scaffold fabrication

The ECM derived scaffolds were fabricated as previously described [23,24,28]. Briefly, for AC-ECM, AC was removed from porcine medial femoral condyles, the starting material for Bone-ECM scaffolds was bovine bone and for GP-ECM, GP cartilage was scraped from the epiphyseal growth plate of porcine femoral heads. After cryomilling the tissues into a powder, tissues were then solubilised in pepsin and acetic acid. Solubilised ECM was salt precipitated and dialysed before freeze-drying to obtain stock which could be then stored long term at -80 °C. To fabricate the scaffolds; the freeze-dried collagenous material was resuspended to a final concentration of 20 mg/ml (2%) in 0.02 M acetic acid. The solution was neutralized with NaOH and crosslinked with 5 mM glyoxal. The ECM slurry was then transferred to custom-made moulds, placed in the oven at 37 °C and allow to partially crosslink for 30 min.

Two different moulds and four different freeze-drying protocols were used to fabricate the scaffolds with tailored pore morphology: (i) random standard, (ii) random annealed, (iii) aligned

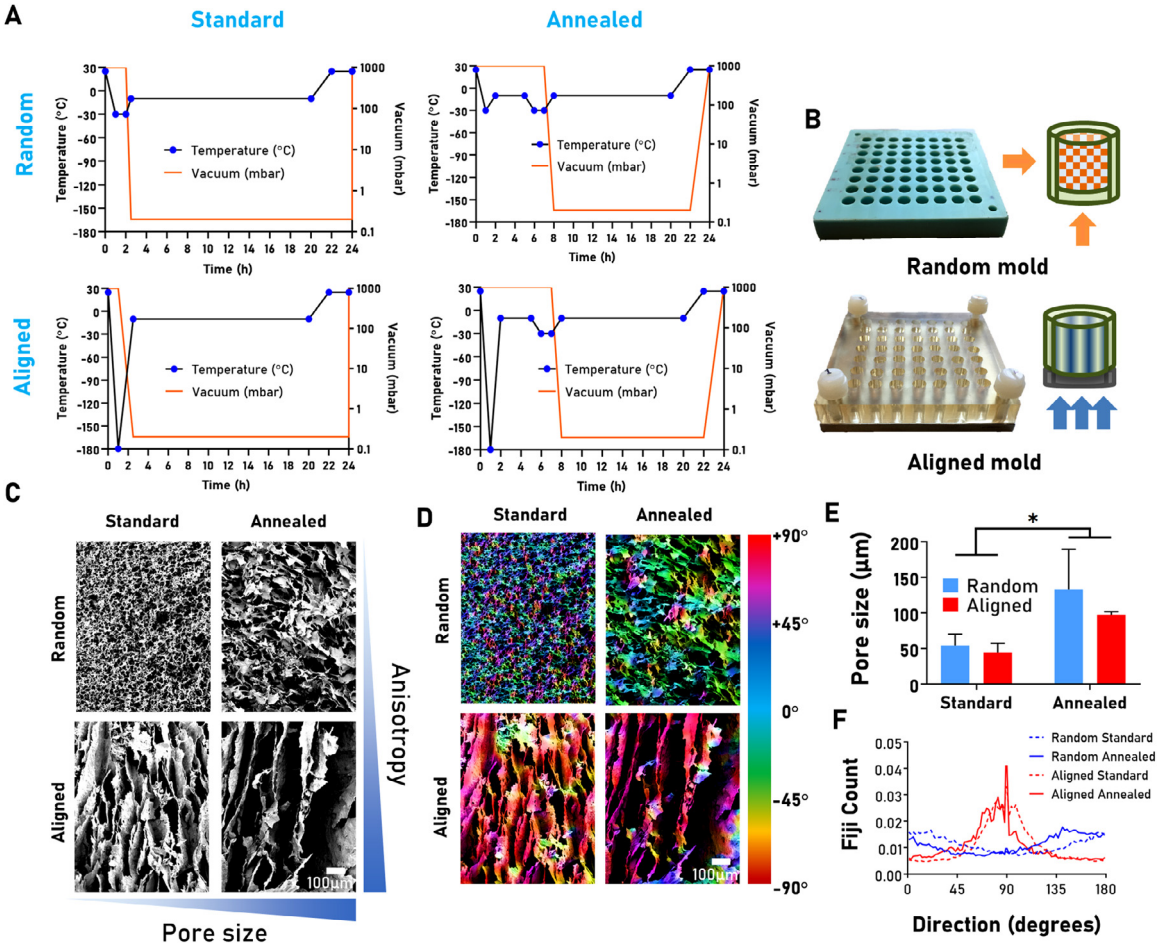

Fig. 1. Characterization of pore morphology in scaffolds fabricated using a freeze-drying protocol combining directional freeze-casting and annealing. Graphical schematics of the temperature and vacuum parameters employed during the 4 different freeze-drying (FD) protocols (A). Tufset polypropylene mould used for the fabrication of scaffolds with random pore shape (above) and the main heat transfer directions that affect the mould. Silicone and metal mould used for aligned pores (below) and main heat transfer direction that affects the mould (B). Scanning electron microscopy images of the scaffolds corresponding to the 4 different FD protocols (C). Overlapping fiber orientation color map showing degree of anisotropy in the ECM derived scaffolds (D). Mean pore/channel diameter comparison for all 4 groups based on SEM image quantification (E). Representative histogram curve of the orientation shown in the color map images where the plugin from Fiji, Directionality, was used to calculate the number of fibres (Fiji count) per direction (degree). (F). *p$P < 0.05$; $n \geq 3$.

standard, (iv) aligned annealed (Fig. 1A). In order to generate random or aligned pores, the heat transfer direction had to be optimized for each case. Multidirectional heat transfer will lead to an isotropic porous structure (random pores), while unidirectional heat transfer will lead to an anisotropic porous structure (aligned pores). In order to generate scaffolds with increased pore size, an annealing step was included in the freeze-drying process. The annealing step consists of holding the product at a temperature above the final freezing temperature for a defined period, which allows the development and growth of already formed ice-crystals during the first freezing step. After freeze-drying, the scaffolds then underwent dehydrothermal (DHT) crosslinking. The DHT process was performed in a vacuum oven (VD23, Binder, Germany), at 115 °C, in 2 mbar for 24 h, as previously described [23].

2.2. Bilayer (AC:Bone) ECM scaffold fabrication

Tissue-specific bilayer scaffolds were made with two distinct layers of solubilized ECM materials: articular cartilage (AC) and bone. The fabrication method was adapted from the protocol described above. Briefly, after the solutions were partially crosslinked with 5 mM glyoxal at 37 °C for 30 min the Bone-ECM slurry was poured onto the mould allowing unidirectional heat transfer (metal base + Polydimethylsiloxane (PDMS) wells) and frozen for 2 min with liquid nitrogen. Then, the AC-ECM slurry was poured on top and allowed to equilibrate for 10 min. The mould was then placed in the freeze-drier and the aligned annealed protocol as described in Fig. 1A was used. After freeze-drying, the scaffolds were removed from the mould and subjected to DHT treatment as above.

2.3. Pore morphology characterization

Prior to scanning electron microscopy (SEM), scaffolds were sputter coated with a gold/palladium alloy (Agar Scientific, UK) for 90 s at 0.1 mBar. SEM images were obtained using a Tescan Mira XMU system with an acceleration voltage of 5 kV and working distance of 5 mm. SEM images of the freeze-dried scaffolds were used to quantify pore size and pore alignment. 'OrientationJ' and 'Directionality' plugins, from ImageJ, were used to create the colour maps of the pore orientation and to generate data to plot the directionality curves, respectively [42].

2.4. Cell culture

For *in vitro* studies, porcine bone marrow mesenchymal stromal cells (MSCs) were freshly isolated from the femurs of 3-4 month old female pigs that were obtained from a local abattoir (Perma Pigs Ltd.). Cell isolation took place approximately two hours post

euthanasia. MSCs were seeded at a density of 500,000 cells per scaffold (1,000,000 MSCs per bilayer scaffold), as previously described [22]. Before supplementing the media, the cells were allowed to attach to the scaffolds for 2 h in the incubator at 37 °C.

For the murine subcutaneous implantation study, 500,000 human bone marrow derived mesenchymal stromal cells (purchased from Lonza) were seeded per scaffold the evening prior to surgery. The MSCs were isolated from a healthy male donor (19 years old) and tri-linage differentiation was performed to confirm tripotentiality (data not shown). Constructs were maintained in expansion media: DMEM + GlutaMAX^{TM}, 10% fetal bovine serum (Gibco®) with 100 units/ml Penicillin, 100 units/ml Streptomycin (Gibco®) overnight before surgery.

To assess cell infiltration, the constructs were kept for 7 days in normoxic conditions (20% O_2 and 5% CO_2) at 37 °C supplemented with 5 ml of expansion media.

To assess cell differentiation and tissue deposition, the constructs were cultured in either (i) chondrogenic media: Dulbecco's modified eagle's medium (DMEM) + GlutaMAX^{TM} (Gibco®), 1 mM sodium pyruvate, 350 µM L-proline, 1.5 mg/ml bovine serum albumin (BSA), 1 nM dexamethasone, 300 µM ascorbic acid, 17 µM linolenic acid, 10 ng/ml transforming growth factor β3 (TGF-β3, (Peprotech) 1X insulin-transferrin-selenium; or (ii) osteogenic media: DMEM + GlutaMAX^{TM}, 10% fetal bovine serum (Gibco®), 10 mM β-glycerophosphate, 1 nM dexamethasone, 90 µM ascorbic acid. All media were supplemented with 100 units/ml Penicillin, 100 units/ml Streptomycin (Gibco®) and 0.25 µg/ml amphotericin B.

Samples at day 0 (after cell seeding) and day 28 were biochemically analysed for DNA, sulphated GAG (sGAG), collagen content and calcium deposition. The DNA content was quantified by Bisbenzimide Hoechst assay. sGAG content was quantified by dimethylmethylene blue dye-binding assay (Blyscan, Biocolor Ltd, Northern Ireland), using bovine chondroitin sulphate as the standard. Collagen content was indirectly determined by measuring the hydroxyproline (HxP) content after acidic hydrolysis of the samples at 110 °C for 18 h in 38% HCl. Collagen content of scaffolds was quantified by measuring total hydroxyproline content as previously described [43]. A hydroxyproline:collagen ratio of 1:7.69 was assumed to determine the collagen content [44]. Calcium content was determined using the o-cresolphthalein complexone (oCPC) method (Sentinel Diagnostics) according to the manufacturer's instructions.

2.5. Live/dead imaging

Constructs were transferred to a 24 well plate and washed thoroughly in PBS. The constructs were sliced in the longitudinal direction (so the microscope imaging can take place in the middle of the construct). 1 ml of the freshly prepared Live/Dead solution was added to each well consisting of 20 µL of 2 mM Ethidium homodimer with 4 µL of 4 mM Calcein AM (both Cambridge Biosciences) in 10 mL PBS. After incubation for 1 h, the scaffolds were washed three times with PBS. Finally, the constructs were imaged using a Leica SP8 scanning confocal microscope. The percentage of live/dead cells was obtained using Image J to count the green (alive) or red (dead) cells.

2.6. Histological analysis

ECM derived constructs (2 scaffolds at each time point) were fixed overnight prior to dehydration in increasing alcohol solutions and xylenes and finally embedded in paraffin. The wax-embedded constructs were sectioned (6 µm slices) using a microtome. Sections were rehydrated and stained with alcian blue for sGAG, with picrosirius red for collagen, with alizarin red for calcium. Immunohistochemical analysis of collagen types I, II and X was performed as previously described, details of specific antibodies can be found in Supplementary table 1 [23]. Picro-sirius red stained samples were imaged under polarized light microscopy (PLM) to investigate collagen fibre orientation. PLM images were further analyzed with Directionality and Orientation J plugins for Image J in order to characterise the degree of orientation as previously described [22].

2.7. Mouse subcutaneous implantation

All animal experiments were conducted in accordance with the recommendations and guidelines of The Health Products Regulatory Authority (HPRA), the competent authority in Ireland responsible for the implementation of Directive 2010/63/EU on the protection of animals used for scientific purposes in accordance with the requirements of the Statutory Instrument No. 543 of 2012.

Mouse procedures were ethically approved by both the animal research ethics committee of Trinity College Dublin and the HPRA under protocol number AE19136/P069. 8-week old BALB/c OlaHsd-Foxn1^{nu} nude mice (Envigo, Oxford, UK) were anaesthetised using a mixture of xylazine (10 mg/kg) and ketamine (100 mg/kg) given subcutaneously before surgery. Once anaesthetised, analgesia in the form of 5 mg/kg carprofen was also administered subcutaneously. Two incisions were made in the skin slightly lateral to the spine of each animal and four subcutaneous pockets were created. MSC seeded ECM constructs were then implanted, 4 constructs per animal, $n = 8$ per experimental group. To ensure the mechanically soft ECM scaffolds maintained their shape while implanted, the scaffolds were deposited into a cylindrical 3D printed polycaprolactone (PCL- Perstop) sheath (wall thickness = 0.25 mm; diameter = 4 mm; height = 4 mm) as previously described [45]. Experimental groups and implantation position was randomized for each animal. After 8 weeks, animals were euthanized by CO_2 asphyxiation. Post-surgery and before fixation, gross morphological images were taken with a digital microscope system (Ash Inspex HD 1080p) for macroscopic evaluation. Samples were then incubated in paraformaldehyde for 24 h to fix before using microcomputed tomography (µCT) to scan the samples at 55 kVp, 145 µA and a 12 µm voxel size using a MicroCT42 system (Scanco Medical). Subsequently, samples were then processed for histology, sectioned at 10 µm and stained with Masson's Trichrome to examine tissue deposition. Masson's Trichrome sections were taken from the center of the constructs; dark green stain corresponds to new mineral deposition, light green is collagen and red is muscle or blood vessels.

2.8. Osteochondral caprine model

Caprine procedures were approved by both the University College Dublin Animal Research Ethics Committee (AREC-18-17) and the Irish Health Products Regulatory Authority (AE18982/P142).

The surgical procedure in the caprine model was carried out as previously described [22]. Briefly, the goats were premedicated with diazepam (0.4 mg/kg IV) and butorphanol (0.4 mg/kg IV). Once sedation was achieved a lumbosacral epidural block was administered using a combination of lidocaine (2 mg/kg) and morphine (0.2 mg/kg). Following placement of an intravenous catheter, anesthesia was induced with propofol on effect (maximum dose 4 mg/kg IV). Anesthesia was maintained using isoflurane in 100% oxygen with ventilation to maintain normal end tidal CO_2 between 4.6 and 6 kPa. Lactated Ringer's solution was infused at 10 ml/kg/h. Following induction of anesthesia, the goats were placed in dorsal recumbency on a heat mat and an arthrotomy of each stifle joint was then performed using the lateral para-patellar approach.

A critically sized circular osteochondral defect, 6 mm in diameter × 6 mm in depth, was created in the left and right lateral trochlear ridge of the distal femur using a hand drill, a pointed and flattened drill bit and a depth guide. During the drilling process extensive irrigation and flushing with saline fluids (0.9% NaCl) is performed to prevent heat production and accumulation of drilling debris in the joint. The stifle joints were randomly assigned to one of the two treatment groups: (1) Empty control and (2) AC-Bone ECM derived bilayer scaffold. The bilayer scaffold was press fit into the defect site cell-free before routine closure of the joint capsule, subcutaneous tissues and skin with sutures. Morphine (0.2 mg/kg IM) and non-steroidal anti-inflammatory drug meloxicam (0.5 mg/kg SC) were administered at the end of anesthesia. Following surgery, goats were group housed in indoor pens to allow skin incisions to heal and were allowed full weight bearing immediately. During this period the animals were closely monitored to ensure adequate analgesia and optimal welfare. Daily meloxicam and antibiotics (Amoxicillin clavulanic acid 8.75 mg/kg) were administered for 5 days post-surgery. Two weeks post-operatively, following removal of sutures, animals were let out to pasture for the remainder of the study period. Euthanasia was carried out with an overdose of sodium pentobarbital (Euthatal) administered by IV injection after 6 months post-implantation ($n = 8$) to permit harvesting of the treated joints.

2.9. Repair tissue evaluation

1.5 cm^3 sections containing the defect site were harvested from the goats using an oscillating bone saw. Before fixation, gross morphological images were taken with a digital microscope system (Ash Inspex HD 1080p) for macroscopic evaluation. Macroscopic images were blinded, randomised and subsequently scored by four expert reviewers using a previously described macroscopic scoring system as shown in supplementary Table 2 [46,47]. Levels of mineralization within the repair tissue (5 mm diameter cylindrical region) was quantified using µCT (Scanco Medical, Switzerland) at a threshold of 210, corresponding to a density of 399.5 mg hydroxyapatite/cm^3. Two regions of interest for calculating bone density (bone volume per total volume) were defined as follows: The subarticular spongiosa (SAS) defined as the bottom 3 mm of the bony region of the defect) and the subchondral bone plate (SBP) defined as the upper 1 mm of the bony region of the defect. For histological analysis, samples were fixed in 10% neutral buffered formalin solution (Sigma) for 72 h with agitation. Samples were then decalcified with decalcifying solution lite (Sigma) until all mineral was removed, which was confirmed by x-ray analysis. Demineralized wax-embedded constructs were sectioned at 10 µm and stained with safranin O and picrosirius red. Histological scoring was performed using a modified ICRS II scoring system [48]. Safranin O staining was also used in combination with Image J to quantify the area of positively stained cartilage within the defect site. Picrosirius red stained samples were imaged under polarized light microscopy to investigate collagen fibre orientation. The Directionality plugin for ImageJ [42] was used to quantify the mean orientation and angular dispersion of the collagen fibres observed in the superficial and deep zones of the regenerated AC as previously described [22]. The angular dispersion is a measure equivalent to the standard deviation of the orientation value given by Image J. Therefore, it can be considered a measure of the variability in the fibre orientation. A low value indicates that most of the fibres are oriented with the mean fibre direction. Immunohistochemistry was performed for collagen type II (Santa Cruz- sc52658 1:400) as previously described [23]. For the detection of Lubricin, antigen retrieval was performed using Chondroitinase ABC (0.25 units/ml - Sigma) for 60 min at 37 °C. Non-specific binding was blocked using a solution of 1% bovine serum albumin (Sigma) and 10% donkey serum (Sigma) in PBS for 60 min. Anti-lubricin primary antibody (Millipore MABT400 1:500 dilution) was then incubated on the samples overnight at 4 °C. Endo-peroxidase activity was quenched using 3% hydrogen peroxide solution (Sigma). Next, the secondary antibody (Anti-IgG mouse (Sigma B7151, 1.5:200 dilution) was incubated on the samples for 60 min at room temperature. Staining was developed using a DAB (3,3′-Diaminobenzidine) substrate kit (Vector Labs). To quantify the extent of positive type II collagen staining in the defect site defect, a 1.5mm x 5 mm region of interest central to the defect was selected and DAB (3,3′-Diaminobenzidine) positive staining was quantified using the plugin IHC profiler for ImageJ [49]. A grading using the terms: worst, intermediate and best was used to refer to the representative images picked to display the histological data in the figures. This grading is based on the corresponding analysis and scoring (reflected in the same figure).

2.10. Statistical analysis

Results are presented as mean +/- standard deviation. Statistical analysis was performed using Graph Pad Prism 9 (San Diego, USA). Statistical differences were analysed by one-way or a two-way analysis of variance (ANOVA) with Tukey's test for multiple comparisons to compare experimental conditions or in the case of comparing two experiment groups a paired or unpaired t-test was used when appropriate. Statistically significant changes are marked as $^{*} = p < 0.05$; $^{**} = p \leq 0.01$; $^{***} = p \leq 0.001$.'

3. Results

3.1. Directional freeze-casting and annealing enables the fabrication of ECM derived scaffolds with tailored pore shape and size

Porous anisotropic scaffolds were produced using solubilized AC-ECM by (i) modifying the freeze-drying kinetics (Fig. 1A) during the fabrication procedure and (ii) by controlling the direction of heat transfer during the freezing step before freeze-drying using moulds which permits heat transfer in all directions (random) or preferentially along the vertical axis (aligned) (Fig. 1B). Scanning electron microscopy (SEM) was used to characterize the morphology (diameter and alignment) and distribution of the channels/pores in both scaffold types (Fig. 1C–F). The mean pore diameter for the standard random scaffolds was 54 ± 13 µm, increasing to 133 ± 56 µm for the annealed random scaffolds (Fig. 1E). They were comparable to that observed in the aligned scaffolds, where the mean pore diameter for the standard scaffolds was 44 ± 11 µm, increasing to 97 ± 4 µm for the annealed scaffolds (Fig. 1E). The OrientationJ and directionality plugins for ImageJ were used to quantify the degree of pore anisotropy (Fig. 1F). There was no obvious preferential pore alignment in any particular direction in the AC-ECM scaffolds fabricated using the traditional mould (random scaffolds). Conversely, an aligned honeycomb-like pore architecture was observed in the scaffolds fabricated by directional freeze-drying (aligned scaffolds).

3.2. Increased scaffold pore size promotes enhanced cell infiltration and homogenous tissue deposition

The standard and annealed AC-ECM scaffolds were next seeded with MSCs to assess the influence of pore size on cell infiltration and matrix deposition. After seeding, cell infiltration into the centre of the scaffold was more noticeable in the annealed scaffolds with larger pores. It should be noted that the displayed images correspond to transversal cross-sections of the samples (Fig. 2A). SEM images of the scaffolds at day 0 confirm the larger pore sizes in

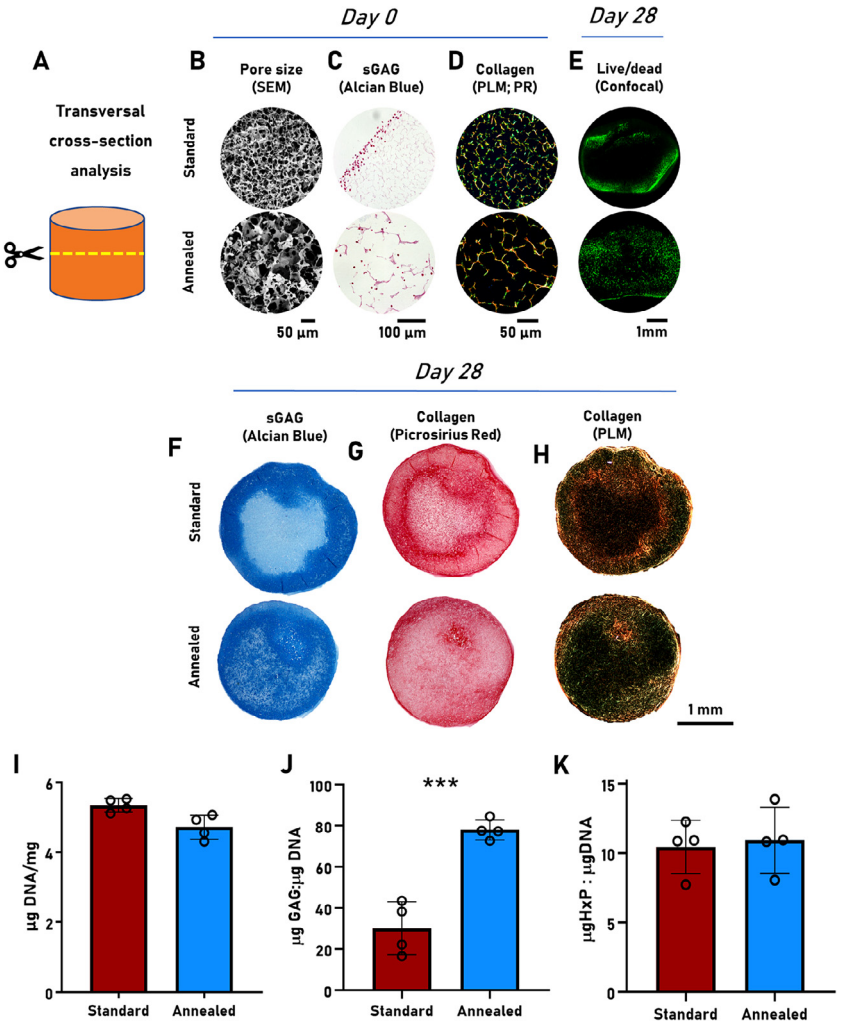

Fig. 2. Effect of pore size on chondrogenesis of MSCs in AC-ECM scaffolds (random standard Vs random annealed). Schematic illustrating the transversal cross section cut employed for histological analysis (A). Scanning electron microscopy (SEM) images of scaffolds fabricated with standard or annealed protocols (B). Histological analysis of day 0 samples with alcian blue for sGAG staining (C). Polarized light microscopy (PLM) image of picrosirius red staining at day 0 (D). Live/dead images of MSC seeded scaffolds after 7 days in expansion medium (E). Histological analysis of day 28 samples cultured in chondrogenic medium with alcian blue for sGAG staining (F), picrosirius red (PR) for collagen staining (G) and Polarized light image to visualize collagen fibre directionality (H). Biochemical analysis of DNA (I), sGAG:DNA ratio (J) and HxP:DNA ratio (collagen) at day 28 (K). *** $pP < 0.001$; $n = 4$.

the annealed scaffolds (Fig. 2B). Histological analysis at day 0 confirmed that the majority of cells (nuclear fast red counterstained) agglomerated along the perimeter of the standard scaffold with smaller pores, while there was greater cell infiltration into the centre of the scaffolds with the larger pores (Fig. 2C). In addition, bright field microscopy combined with picrosirius red staining confirmed the collagenous nature of the AC-ECM scaffolds (Fig. 2D), with a noticeable increase of orange color in scaffolds with bigger pores as a result of the cryocondensation of the material during the annealing process. Confocal images, after 7 days of culture, demonstrated an increased number of live cells (stained with calcein) in the centre of the annealed scaffolds with large pores than in the standard scaffolds with smaller pores (Fig. 2E). After 28 days of culture in chondrogenic media, a more homogenous distribution of sGAGs and collagen was observed in the annealed (large pore) scaffolds (Fig. 2F and G). Polarized light microscopy was able to detect birefringent fibres in both scaffolds demonstrating mature collagen deposition (Fig. 2H). There was no significant difference in the amount of DNA levels or collagen deposited in the two scaffold types (Fig. 2I and K). Significantly higher levels of sGAG deposition was observed in the annealed scaffolds with larger pores compared to standard scaffolds with smaller pores (Fig. 2J).

3.3. An anisotropic scaffold pore morphology supports oriented tissue deposition

To assess the influence of scaffold pore architecture on cartilage tissue formation *in vitro,* MSCs were seeded onto annealed random or annealed aligned scaffolds and cultured in chondrogenic media for 28 days. Again, it should be noted that the displayed images correspond to longitudinal cross-sections of the samples (Fig. 3A). Macroscopic images of the scaffolds at day 0 (before cell seeding) displayed a light-orange color (as scaffolds are fabricated with phenol red-containing medium) with visible architectural differences observed between the two scaffolds (Fig. 3B). At day 0, the scaffolds stained weakly for sGAG (Fig. 3C), but positively for collagen (Fig. 3D). After 4 weeks of culture, histological analysis demonstrated the homogenous deposition of cartilaginous tissue, rich in sGAGs and type II collagen, throughout both scaffolds (Fig. 3E–G). Only weak staining for type X collagen (a hypertrophic marker) was observed in both scaffolds (Fig. 3H). Polarized light microscopy was undertaken to characterise collagen alignment in both scaffolds (Fig. 3I). Magnified pictures were taken of two regions of interest (ROI) in the scaffolds: one at the periphery and one in the centre designated as the top and middle ROIs.

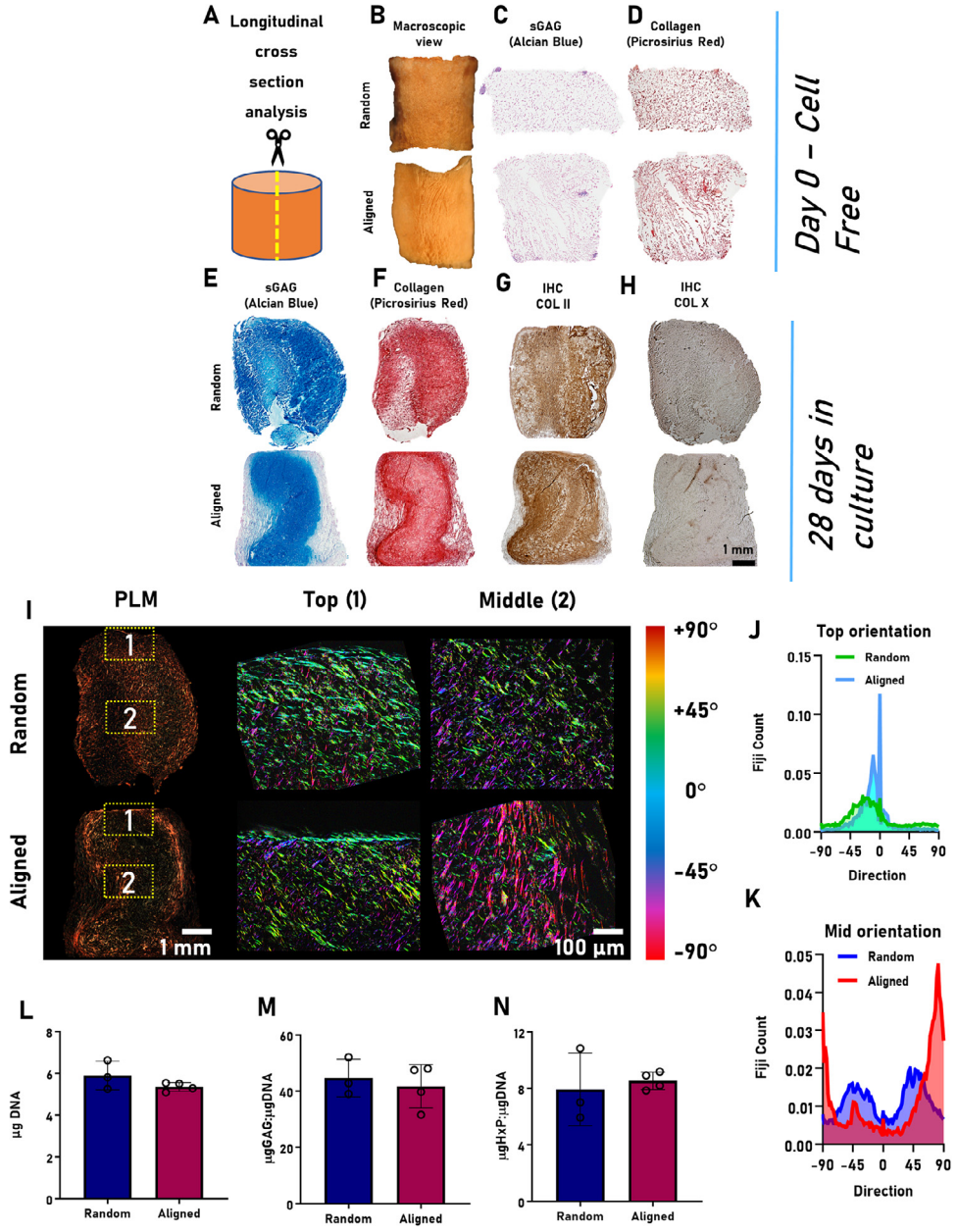

Fig. 3. The effect of pore architecture on chondrogenesis of MSCs (random annealed Vs aligned annealed) in AC-ECM scaffolds. Schematic illustrating the transversal cross section cut employed for histological analysis (A). Macroscopic images of random and aligned scaffolds (B). Histological analysis at day 0, showing alcian blue for sGAG staining and picrosirius red staining for collagen (C+D). Histological analysis of day 28 samples cultured in chondrogenic medium, showing alcian blue for sGAG staining (E), picrosirius red for collagen (F), immunohistochemistry for collagen type II and X (G+H). Collagen alignment analysis by polarized light microscopy (PLM), two regions of interest (ROI) are highlighted by dashed yellow square: at the top and middle of the scaffolds highlighting the regional differences in fiber alignment (I). Representative histogram curves of the orientation shown in the color map images where the plugin from Fiji, Directionality, was used to calculate the number of fibers (Fiji count) per direction (degree) (J+K) Biochemical analysis of day 28 constructs demonstrated no significant changes in DNA (L) sGAG:DNA ratio (M) HxP:DNA ratio (collagen) (N). $n = 4$.

While the top of both scaffolds was characterised by the presence of collagen fibres parallel to the surface, collagen alignment differed within the middle of the two scaffolds. Collagen fibres appeared to be randomly distributed within the scaffold with random pores. In contrast, the collagen fibres appeared to be preferentially deposited parallel to the long-axis of the pores within the aligned scaffold. Directionality analysis confirmed very distinct collagen fibre alignments, particularly in the middle ROI in the scaffold with aligned pores (Fig. 3I). Biochemical analysis validated histological results and demonstrated that there was no significant difference in the DNA, sGAG and collagen content of scaffolds with random and aligned pores (Fig. 3J-I).

3.4. *Bone-ECM scaffolds promote robust mineralization* in vivo

Having demonstrated that the pore architecture of AC-ECM scaffolds could be augmented to enhance both cellular infiltration and cartilage matrix deposition, we next sought to fabricate an osteo-inductive ECM scaffold that could later be coupled to the optimized AC-ECM scaffold to generate a bilayered scaffold for osteochondral defect repair. To this end, we fabricated three scaffolds using the same solubilization procedure from growth plate (GP), AC and bone source tissues. To evaluate the ability of these three scaffolds to support osteogenesis *in vivo*, they were seeded with human BM-MSCs and implanted subcutaneously in nude mice for

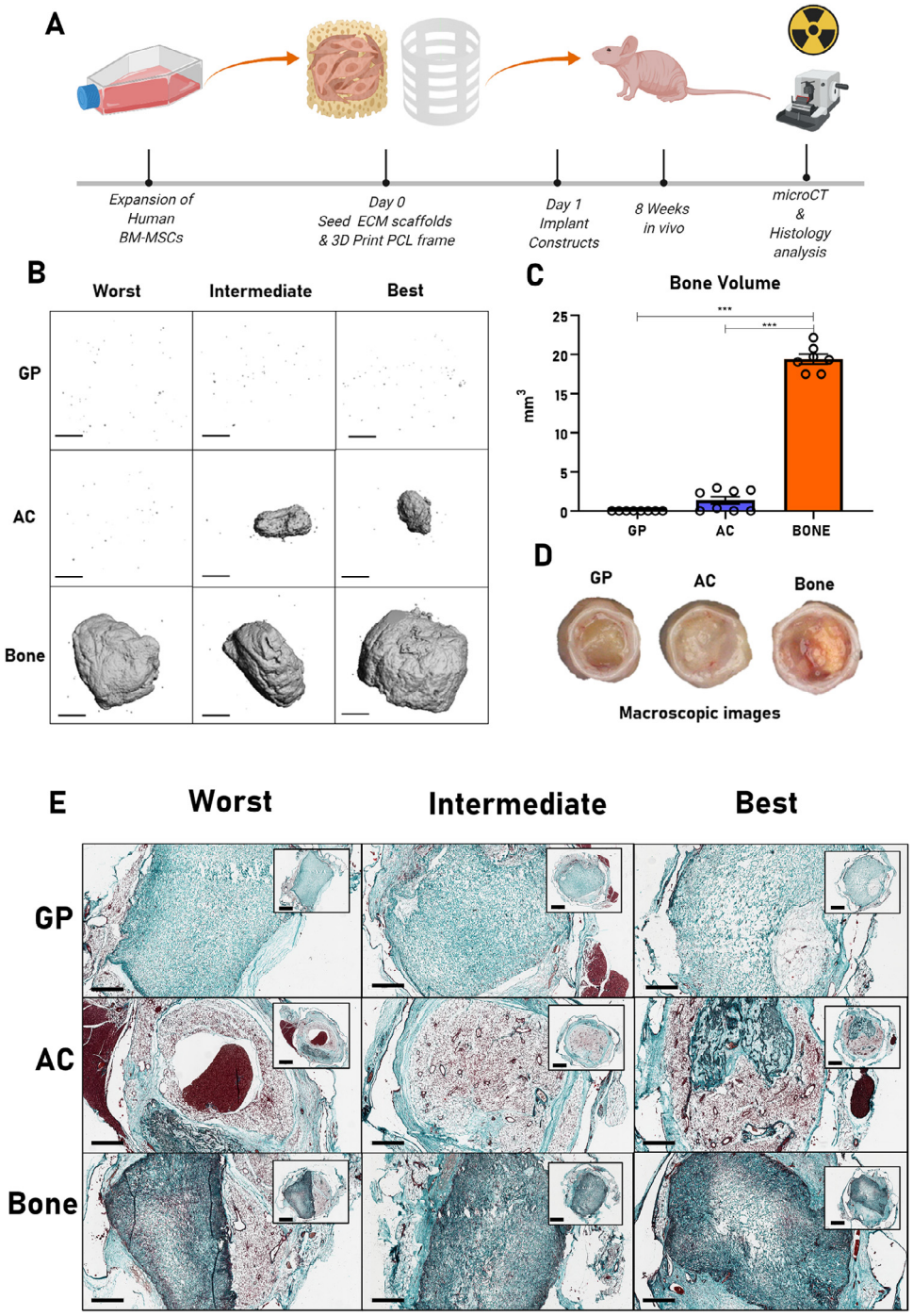

Fig. 4. Bone-ECM scaffolds seeded with MSCs promoted the greatest levels of mineralization in a mouse subcutaneous model. Schematic illustrating the timeline for the *in vivo* study (A). µCT 3D reconstructions of the excised constructs after 8 weeks *in vivo*, scale bars = 1mm (B). Quantification of total volume of excised constructs obtained from µCT scans (C). Macroscopic images of GP, AC and Bone-ECM constructs after 8 weeks (D). Masson's Trichrome histological staining of sections taken from the center of the constructs; dark green stain corresponds to new mineral deposition, light green is collagen and red is muscle or blood vessels (E). Scale bars in histology = 500 µm or 1 mm. *** $pP < 0.001$; $n = 8$.

8 weeks. A schematic of the experimental design can be seen in Fig. 4A. Due to the relatively weak mechanical properties of the ECM scaffolds, each scaffold was encompassed in a 3D printed PCL sheath to prevent the scaffold being crushed. µCT reconstructions of the excised constructs after 8 weeks revealed stark differences in the amount of mineral deposited in the different scaffolds (Fig. 4B). Significantly greater bone volume was observed in the Bone-ECM constructs when compared to both GP-ECM and AC-ECM scaffold groups (Fig. 4C). Macroscopically, visible differences in tissue deposition were observed. Both GP-ECM and AC-ECM constructs generally consisted of a weak, fibrous tissue, while the Bone-ECM constructs contained solid, vascularized tissue (Fig. 4D). Histological analysis of the constructs revealed that GP constructs showed minimal, if any, *de novo* bone tissue formation with the collagen matrix of the scaffold, which was still clearly visible after 8 weeks. AC-ECM constructs supported variable and minimal mineral formation *in vivo,* with only 50% of the constructs containing small mineral deposits. Within the Bone-ECM constructs,

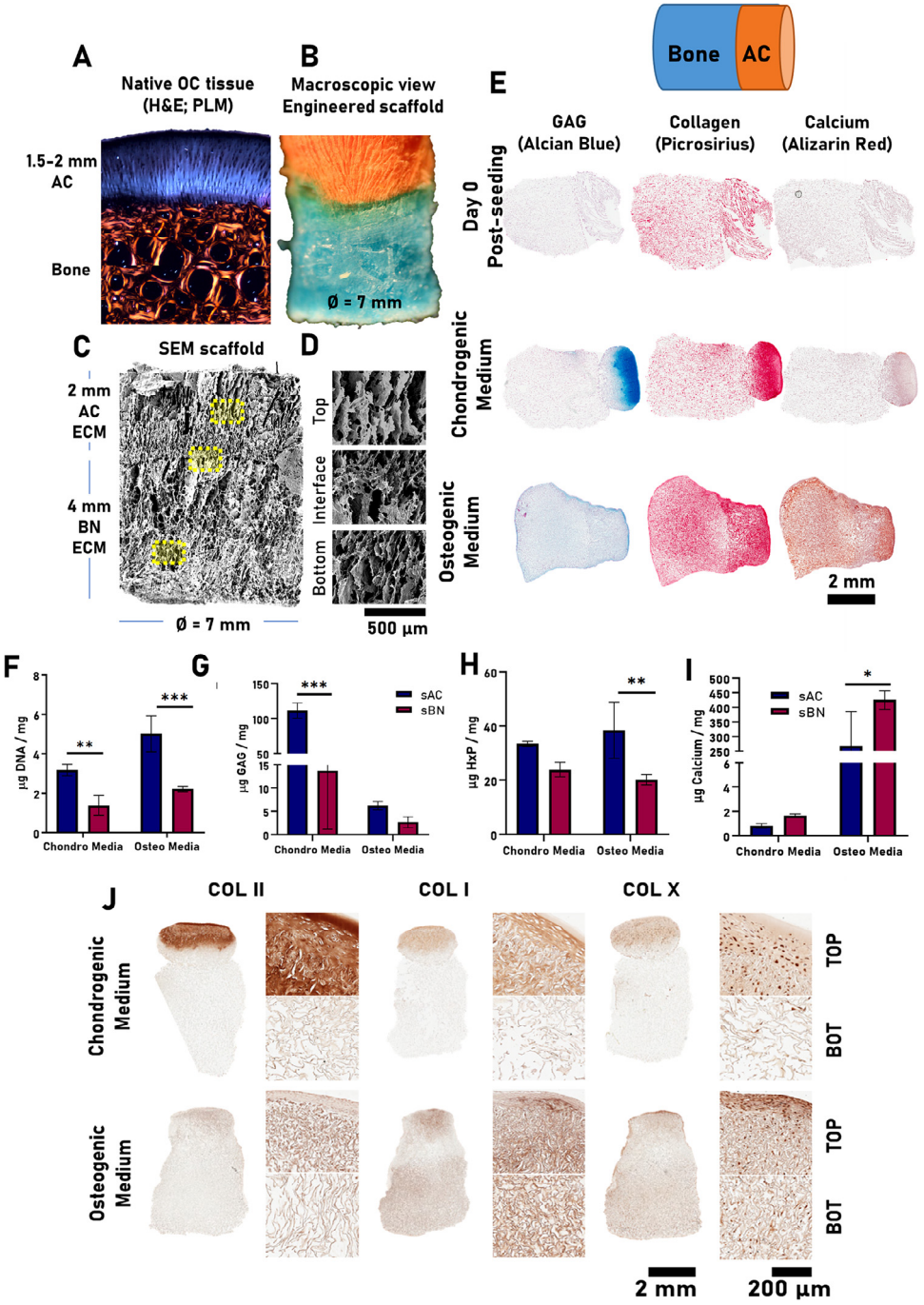

Fig. 5. Spatial differentiation of MSCs on a bilayered osteochondral scaffold *in vitro*. Hematoxylin and eosin (H&E) stained histological section of native osteochondral goat tissue visualized with polarized light microscopy (PLM) (A) Macroscopic image of the bilayer scaffold, ECMs were dyed with food coloring prior to fabrication to aid visualization of distinct layers (B). Scanning electron microscopy images of the fabricated bilayer scaffold, top layer corresponding to articular cartilage AC-ECM and bottom layer, to bone-ECM (C+D). Histological analysis at day 0 and day 28 of culture in either chondrogenic medium (CM) and osteogenic medium (OM): alcian blue for sGAG, picrosirius red for collagen, alizarin red for calcium staining (E). Day 28 constructs cultured in either CM or OM were biochemically analyzed to determine DNA (F), sGAG (G), collagen (H) and calcium content (I). Immunohistochemistry analysis at day 28 of samples cultured in either CM or OM for specific deposition of collagen types I, II and X (J) * $p < 0.05$, ** $p < 0.01$, *** $p < 0.001$ $n = 3$.

robust mineralization was observed in all constructs histologically, which correlated with the µCT findings (Fig. 4E).

3.5. Bilayered scaffolds consisting of tissue-specific ECM support spatially defined chondrogenesis and osteogenesis

Next, we fabricated a bilayered scaffold composed of a base layer of solubilized bone-ECM and an overlying layer of solubilized AC-ECM, mimicking the native OC tissue structure (Fig. 5A). The scaffolds were fabricated with aligned annealed pores to firstly support the migration of cells from the osseous to the chondral region of the scaffold, and secondly to support the development of structurally organised AC. Food colorant was used during the fabrication process to demonstrate the integration between the two distinct layers (Fig. 5B). These bilayer scaffolds were then seeded with MSCs and maintained in either chondrogenic or osteogenic media. After 28 days of culture in chondrogenic medium, the top layer (AC-ECM) stained strongly with alcian blue and picrosirius

red, indicating robust sGAG and collagen deposition. On the other hand, only weak staining for sGAG and collagen deposition was observed in the bottom layer (Bone-ECM). Both layers stained negative for alizarin red, indicating no mineralisation of the scaffolds (Fig. 5E). In osteogenic medium, neither layer was shown to stain strongly for sGAG. Both layers stained strongly for collagen and mineral deposition (Fig. 5E).

DNA levels were significantly higher in the AC-ECM layer than in the Bone-ECM layer in both chondrogenic and osteogenic media (Fig. 5F). sGAG deposition was higher in the AC layer in chondrogenic conditions (Fig. 5G). The highest levels of collagen deposition occurred in the AC layer of scaffolds cultured in osteogenic medium (Fig. 5H). Very low levels of calcium deposition were observed at day 28 in samples cultured in chondrogenic medium. In contrast, robust calcium deposition was observed in constructs cultured in osteogenic medium, with significantly higher levels measured in the Bone-ECM layer (Fig. 5I).

Immunohistochemistry was used to assess the different types of collagen deposited in each scaffold layer in the different media conditions. When constructs were cultured in chondrogenic media, the AC layer stained strongly for collagen type II. There was however, weak positive staining for collagen type I. Collagen type X deposition appeared localised to the pericellular area. The bone layer did not stain positive for collagen type II or type I deposition, although some weak positive staining for collagen type X was observed (Fig. 5J). In osteogenic medium, negligible staining for collagen type II was observed in both layers. Positive staining for both collagen type I and type X was observed in the AC-ECM layer. The Bone-ECM layer also stained positive for collagen type I, indicative of supporting direct intramembranous ossification (Fig. 5J).

3.6. Evaluation of osteochondral defect repair in a clinically relevant large animal model

Having successfully coupled both chondro-inductive and osteoinductive ECM materials together to create a bilayered scaffold capable of promoting MSC differentiation in a zone specific manner *in vitro*, we next sought to test the ability of the bilayered scaffold to promote joint regeneration in a caprine model of osteochondral defect repair. To this end, cylindrical osteochondral defects (6 × 6 mm) were created in the lateral trochlear ridge of both hind limbs in skeletally mature goats. The two hind limbs of each animal were randomly assigned either as 'empty defect' or 'bilayer scaffold' treatment and therefore internally (i.e. within animal) controlled. Bilayered scaffolds were implanted cell-free as an "off-the-shelf" device. Osteochondral defects were dried with a gauze and scaffolds were inserted into the defect in their dry state. Subsequently, saline was added to the scaffolds so they swelled to fully fill the defect space. A schematic of the surgical procedure can be seen in Fig. 6A. Animals were euthanized after 6 months and the tissue repair evaluated. Macroscopically, variable levels of repair were observed, with some animals having high levels of defect fill across both empty and bilayer scaffold groups (Fig. 6B). When macroscopic scoring was performed by three blinded expert reviewers, no significant differences were observed between the two groups (Fig. 6D). To examine subchondral bone regeneration, 3D μCT reconstructions of the defect site were generated. As with the macroscopic analysis, high levels of variability were observed across the animals (Fig. 6C). In order to quantify the levels of subchondral bone repair, the area was divided into two regions of interest: the subchondral bone plate (SBP, defined as the upper 1 mm of the bony region) and the subarticular spongiosa (SAS, defined as the bottom 3 mm of the bony region). While no significant differences were observed across the groups, the scaffold treated groups visually appeared to develop more consistent subchondral bone repair than the empty defect group, particularly in the SAS region where a trend of increasing bone volume to total volume (BV/TV) ratio was observed (Empty – 25 mm^3 BV/TV; Bilayer scaffold – 31 mm^3 BV/TV; $p = > 0.1$) (Fig. 6C and E).'

We next performed histological analysis to further evaluate the quantity and quality of the newly formed cartilage tissue in the defect sites. Highly variable levels of cartilage matrix deposition were observed in the empty control defects. While all defects were found to be filled with some form of tissue, in the empty group 5 of the 8 animals tested were found to have ≤ 10% of the defect site filled with Safranin-O positive tissue (Fig. 7), indicating little cartilage tissue deposition. In addition, there was a trend towards an increase in subchondral bone abnormalities in the empty defect group when compared to bilayer scaffolds treated defects (Table S1). In animals which received the bilayer ECM scaffold (Fig. 7A), a more consistent level of repair was observed in terms of deposition of sGAG, with only 2 out of 8 animals having ≤ 10% of the defect site filled with Safranin-O positive tissue (Fig. 7B). We also observed Safranin-O positive tissue in the osseous region of several goats in the empty group that was not apparent in the bilayer scaffold treated animals. To further assess the spatial patterns of tissue formation within the osteochondral defects, we quantified the amount of Safranin-O positive staining in a 5 × 5 mm square region of the osseous defect below the chondral region. A trend towards a decrease in Safranin-O positive staining was observed in the animals that received the bilayer ECM scaffold, indicating that tissue remodelling was not completed in the osseous region of the empty cohort (Fig. 7C). Type II collagen, the predominate collagen in native AC, was found to be deposited in both empty and bilayer scaffold treated defects. Upon quantification of the amount of type II collagen positive staining in the cartilage region of interest (5 mm × 1.5 mm), a trend towards increasing type II collagen was observed in the bilayer scaffold treated animals ($p = 0.191$; Fig. 7D).

Having observed increases in chondrogenic matrix protein deposition in the chondral region of bilayer scaffold treated animals, we next examined the superficial zone of the regenerated AC to determine if the bilayered scaffolds were able to recapitulate the specific collagen fibre orientation and lubricin expression associated with this key region in AC. Specific lubricin staining, localized to the superficial zone was only observed in the "best repair" animal of the empty defect group; conversely distinct lubricin staining could be observed in all bilayer scaffold treated animals (Supplementary Fig. 1). Polarized light microscopy of picrosirius red histological stained slides was employed to determine the collagen fibre orientation in the repair tissue. This indicated the development of a more biomimetic collagen organization in the superficial zone of defects treated with the bilayered scaffold, with collagen fibres orientated parallel to the articulating surface (Fig. 8A). The predominant angle of orientation and the dispersion of the collagen fibre orientation were also quantified in the superficial zone. In the superficial zone of native caprine AC, collagen fibres are orientated parallel to the joint surface (1.5° +/- 1.27°), with a low level of fibre dispersion (8.1° +/- 1.3° Fig. 8B); while in the deep zone of native AC, the collagen fibres are orientated perpendicular to the joint surface (87.9° +/- 1.5°), with a low level of fibre dispersion (12.7° +/- 2.2° Fig. 8C). The mean fibre direction and dispersion in defects treated with the bilayered scaffold were more akin to that of the native tissue compared to the empty controls (Fig. 8B). Of note, in the deep zone of the repair tissue, scaffold implantation resulted in a significant increase in the mean fibre direction versus empty controls (Fig. 8C). To better visualize the data, we then plotted the mean fibre dispersion and fibre orientation together with values from representative healthy animals (native tissue). The repair tissue in empty control defects contained a high level of fibre dispersion, with an average fibre orientation angle that noticeably deviated from that observed in the superficial zone of native car-

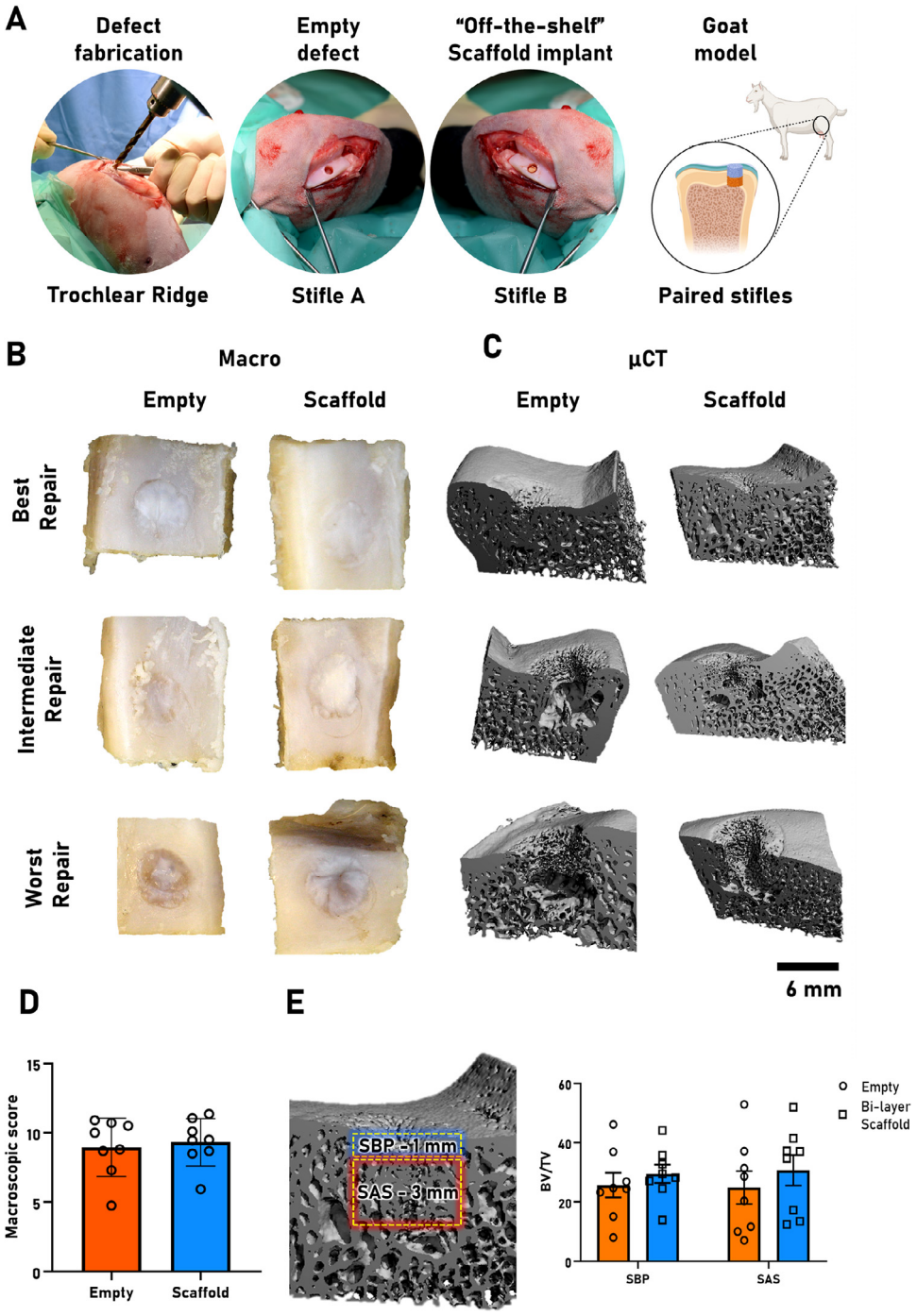

Fig. 6. Preclinical evaluation of the bilayered ECM scaffold in a caprine model of osteochondral defect repair. Schematic diagram illustrating the creation of the defect in the trochlear ridge (A). Macroscopic images for the best repair, intermediate repair and worst repair samples in the empty control and scaffold-treated defects after 6 months (B) µCT 3D reconstructions of the corresponding samples (C). Blinded macroscopic scoring of defect regions (D). Quantification of the bone volume per total volume within two regions of the defect, the upper 1mm subchondral bone plate region (SBP) and the lower 3 mm subarticular spongiosa region (SAS) (E). $n = 8$ animals.

tilage (mean 9.9° +/- 7.5°), as demonstrated by the orange eclipse. In animals treated with the bilayer scaffold, both the average angle of collagen fibre orientation and the levels of dispersion was seen to approach native values, as represented by the blue (bilayered scaffold) and green (native tissue) ellipses.

4. Discussion

The overall goal of this study was to develop an 'off-the-shelf', biphasic regenerative implant for osteochondral defect repair that combines two tissue-specific ECM-derived biomaterials to spatially direct tissue differentiation, with a tailored pore microarchitecture to promote the development of a repair tissue that recapitulates the hierarchical structure of native AC. To achieve this, we successfully developed a freeze-drying method which concurrently increased the mean pore size and introduced an aligned pore orientation. We established that ECM biomaterials derived from solubilized bone were optimal for bone repair applications when compared to scaffolds derived from other musculoskeletal tissues in a subcutaneous mouse model. Finally, we observed that implantation

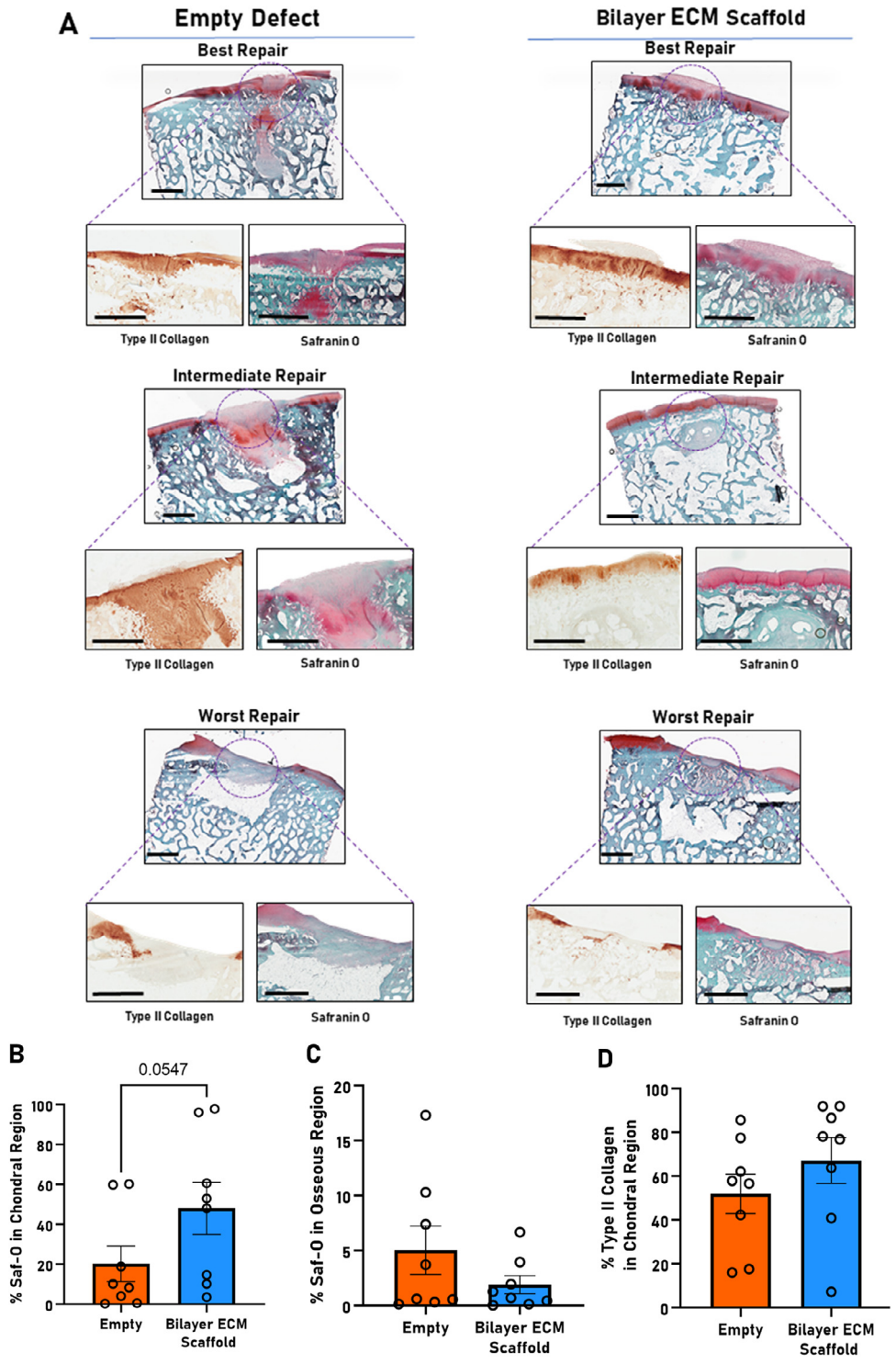

Fig. 7. Histological and immunohistochemical analysis of repair tissue 6 months post-surgery. Safranin-O histological staining and type II collagen immunohistochemistry was performed to evaluate the newly formed cartilage matrix in both the empty defect control group and bilayer ECM scaffold group (A). Bilayer scaffolds promoted deposition of sGAG specifically in the chondral layer. In the chondral layer (5 mm × 1.5 mm), more sGAGs deposition was quantified in the bilayer scaffold group than in empty controls and the inverse was observed in the osseous layer (5 mm × 5 mm) (B and C). Quantification of type II collagen deposition in the chondral region of interest (5 mm × 1.5 mm) (D). Scale bar = 2mm. $^{*}p < 0.05$. $n = 8$ animals.

of an "off-the-shelf" bilayered ECM scaffold improved tissue repair outcomes in a clinically relevant large animal model, specifically the ability to guide neo-tissue organization and therefore recapitulate key aspects of the zonal structure of native articular cartilage.

The *in vitro* and *in vivo* data presented in this study supports the use of tissue-specific ECM scaffolds for orthopedic tissue engineering applications. ECM scaffolds derived from non-tissue specific sources, such as small intestinal submucosa (SIS), have been used for numerous different clinical applications, with at least partial success achieved in the surgical reconstruction of skin, vascular tissue and skeletal muscle among others [50]. It is unlikely, however, that a single source of ECM such as the SIS

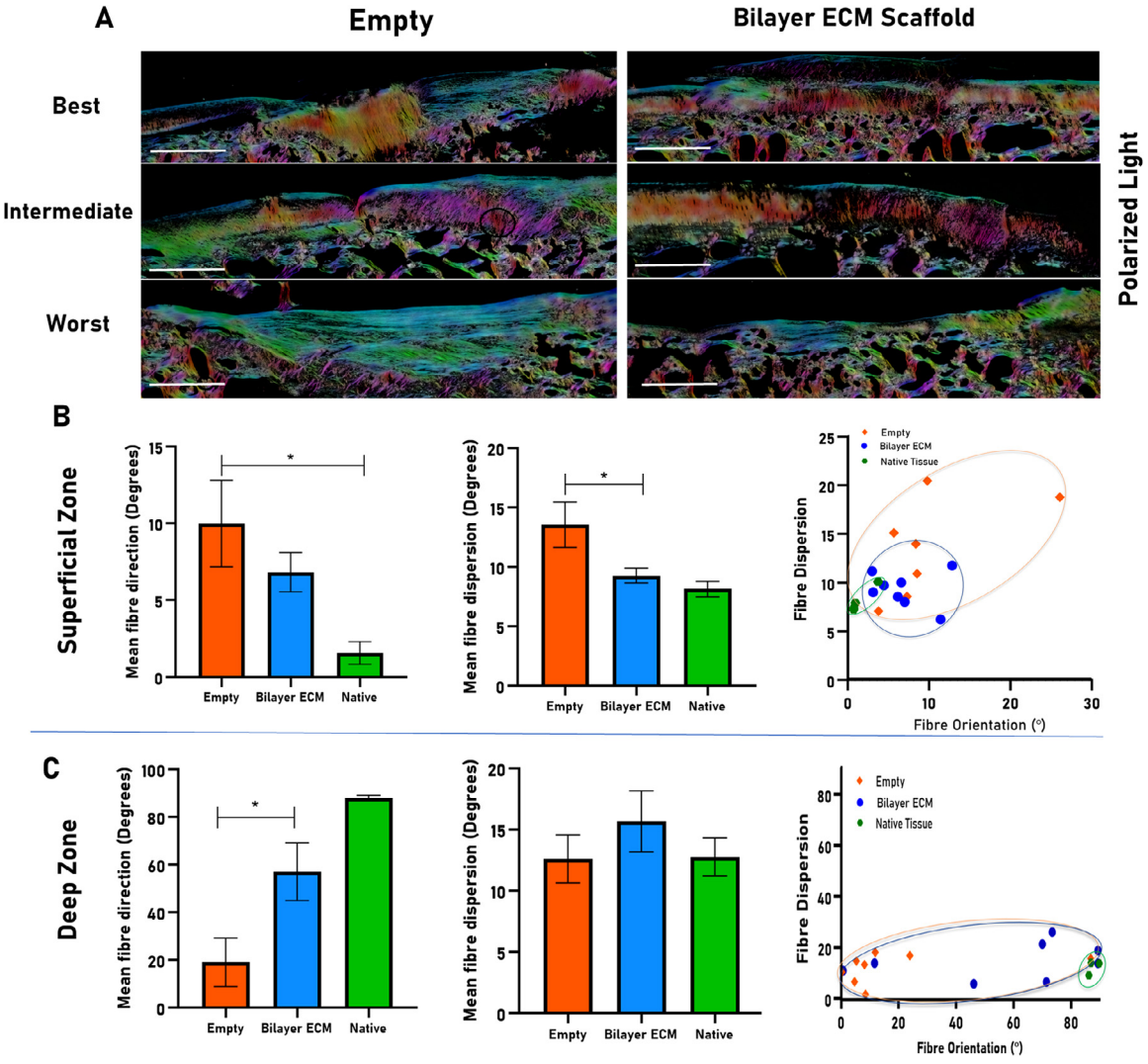

Fig. 8. Bilayered ECM scaffolds promote the recapitulation of native collagen fibre alignment in the superficial and deep zones of the chondral region. Histological sections were stained with picrosirius red and then imaged using Polarized light microscopy. Scale bar = 1 mm (A). The orientation and dispersion of the collagen fibre orientation of the superficial zone of the defect site relative to native controls was plotted. A lower dispersion value indicates higher consistency within the region of interest. Collagen fibres that run parallel to the articulating surface have an orientation of 0°, whereas fibres that are perpendicular to the surface have an orientation of 90° in native caprine cartilage tissue. (B+C). $n = 8$ animals. $^{*}p < 0.05$. Scale bar = 1 mm.

can be successfully used for the successful regeneration of all tissues, and specifically complex interfaces such as the osteochondral unit. We believe that tissue-specific ECM scaffolds, designed with a targeted end application in mind, represent a promising solution to this challenge. Not only can such biomaterials support tissue-specific differentiation of stem/progenitor cells [51–53], but it has also been shown that ECM scaffolds derived from different musculoskeletal tissues can drive distinct macrophage phenotypes [24]. In this study we have successfully demonstrated that such tissue specific ECM derived biomaterials can be combined into a bi-layered scaffold for osteochondral defect repair, where the pore size and architecture was optimized for articular cartilage regeneration.

We observed that an increase in mean pore size, due to the addition of the annealing step during the freeze-drying process, resulted in an increase in cartilage matrix deposition *in vitro*. This result agrees with previous findings where an increase in pore size in collagen-based scaffolds correlated with increased chondrogenic differentiation of MSCs [54–56], however it should be noted that other studies have reported smaller pores can outperform larger pores [57,58] in the context of cartilage tissue engineering. It has also been demonstrated that an increase in pore size can have a detrimental impact on the mechanical properties of porous collagen-based scaffolds [55], however we did not observe significant differences in stiffness following the addition of an annealing step (supplementary Fig. 2). It should be noted that the Young's modulus of our ECM derived scaffolds are relatively low compared to native cartilage tissue. This could potentially be addressed by reinforcing the ECM scaffold with a synthetic polymeric network [28]. We also observed that an aligned pore architecture directed the organization of the collagen fibers laid down locally by resident cells, promoting a more AC-like collagen network both *in vitro* and *in vivo*. Providing such structural cues to cells resident in biomaterial scaffolds will likely be integral to the engineering/regeneration of multiple different tissues.

In order to regenerate both tissues within an osteochondral defect, many consider regeneration of the subchondral bone to be critical as it provides a platform for the regeneration of the overlying AC. With this in mind, this study screened three bone-specific ECM-derived biomaterials to determine the optimal scaffold for the osseous layer of an OC scaffold. While others have observed that AC-ECM scaffolds provide a substrate supportive of endochondral

ossification of MSCs *in vivo* [59], we observed minimal ossification upon subcutaneous implantation of our AC-ECM derived scaffolds. Under osteogenic culture conditions, the GP-ECM scaffolds had previously been shown to support robust osteogenic differentiation when seeded with BM-MSCs *in vitro* [24], but this was not observed here in an *in vivo* environment when exogenous osteogenic factors were not present. The extent of new bone generated *in vivo* in this study compares favorably with similar studies using decellularized bone matrix scaffolds seeded with MSCs in the subcutaneous mouse model [60]. Together these results support the use of bone-ECM as the osseous phase of bilayered scaffolds targeting OC defect repair.

In vitro evaluation of the bilayered scaffold demonstrated zone specific deposition of hyaline-like cartilage matrix in the chondral layer in chondrogenic conditions. Under osteogenic culture conditions, calcium deposition was observed throughout the scaffold, but with significantly more calcium deposition observed in the bone layer. These findings indicate that the bilayer scaffold can promote zone specific differentiation of MSCs, and demonstrate the value of using tissue-specific ECM to support engineering of complex tissues such as the osteochondral unit. This result is in agreement with previous work from our group which demonstrated the ability of scaffolds fabricated from particulated AC and GP to spatially direct MSC differentiation *in vitro* [22]. However, these scaffolds were not solubilized and thus would have maintained high levels of endogenous growth and biochemical factors due to the minimal processing of the tissues. This present study shows that despite the harsh solubilization treatment employed, residual biochemical / physical cues remain in the ECM post fabrication, and that these are sufficient to promote tissue-specific differentiation. The AC-ECM scaffold is predominately composed of type II collagen, which has been shown to promote chondrogenic differentiation in the absence of growth factors [61]. Future studies will seek to elucidate the identity of any residual biochemical cues that remain in the scaffolds post fabrication.

In order to assist potential future clinical translation of this technology, we elected to evaluate the bilayer scaffold in a clinically relevant caprine model of osteochondral defect repair. The goat was selected as the model of choice due to several factors including stifle (knee) size, cartilage thickness, gait and the relative similarity of these metrics to humans [62–65]. The US Food and Drug Administration (FDA) have recognized the goat as one of the most frequently used large animal models for cartilage repair [66,67]. Although this preclinical study was not performed under Good Laboratory Practice (GLP) conditions, the study was designed to follow the ASTM standard F2451-05 “Standard Guide for *in vivo* Assessment of Implantable Devices Intended to Repair or Regenerate Articular Cartilage” where possible and specifically in terms of species used, study duration, defect site and defect generation parameters [62]. Upon examination of the repair tissue 6 months post-surgery, no significant changes were observed in terms of macroscopic evaluation of the defect site and of the total bone formation in the osseous region by µCT evaluation. Although no significant differences were observed by µCT, the bilayer scaffold group supported comparable levels of bone formation to a commercially available scaffold (MaioRegen® (Finceramica [18]) that we have previously tested in this large animal model [22]. Histologically, we observed that our bilayered scaffold treated animals had greater levels of sGAG deposition in the chondral region, and lower levels in the osseous region, when compared to empty controls. These findings demonstrate the capacity of the bilayered ECM scaffolds to support spatially defined tissue development *in vivo*.

The aligned pore architecture of the ECM scaffolds also promoted the development of a more zonally defined AC repair tissue. Specific, distinct lubricin staining could be visualized in the superficial region of defects treated with the bilayered scaffold. Although some specific lubricin staining could be observed in some of the empty control animals with high innate repair capacity, in the majority of cases lubricin deposition was not observed. Lubricin (also known as superficial zone protein (SZP) or proteoglycan 4 (PGR4)) is a key protein in healthy articular cartilage as it is responsible for coating the cartilage surface and providing boundary lubrication, thereby preventing damage to the superficial zone and preserving the chondrocytes beneath [68,69]. In addition to the observation of specific lubricin deposition at the extremity of the superficial zone (lamina splendens), polarized light microscopy and subsequent quantification revealed that the bilayered scaffold supported the development of a more biomimetic collagen fibre network *in vivo* than that observed in the control (untreated) animals. The specific hierarchical structure of AC is responsible for the load bearing, wear resistance and shock absorption properties of the tissue and its regeneration is key to long-term functional regeneration of the tissue [70–72]. Interestingly, statistically significant improvements in both superficial and deep zone fibre alignment parameters were observed as a result of bilayer scaffold treatment, a result that was not observed in our earlier studies using scaffolds that lack such an anisotropic pore architecture [22]. It is also noteworthy that 6 months is a relatively early timepoint for cartilage repair and osteochondral large animal studies; tissue remodelling and regeneration would likely continue for several more months [73]. There are also some limitations with the proposed strategy for joint regeneration that require further consideration. While the *in vivo* outcomes are promising, a consistent quality of repair was not attained, with some animal-to-animal variability observed in both the empty and treatment groups (with some of the empty groups repairing reasonably well). This points to the need for further improvements in the design of ECM-derived biomaterials for the musculoskeletal system. Strategies worthy of future research include the use of host-derived cells for aiding in the repair, regulation of the immune response to favour a pro-regenerative environment, and functionalization of the scaffolds with growth factors known to support hyaline cartilage and bone formation [24,74–76]. In addition to structural regeneration, the repair tissue should also be mechanically functional in order to withstand the challenging loads passing through synovial joints. Future studies are required to assess whether the superior structural repair achieved here translates into improvements in the depth-dependant mechanical properties of the newly formed cartilage. Taken together, the preclinical data presented here demonstrates the ability of bilayered ECM scaffolds with aligned pore networks to support the regeneration of AC that is not only rich in sGAG and type II collagen, but which also mimics key aspects of the zonal nature of the native tissue.

5. Conclusion

The successful treatment of osteochondral defects remains a significant clinical challenge. To address this issue, we have developed a bilayered scaffold for osteochondral defect repair that combines tissue-specific ECM-derived biomaterials to spatially direct stem/progenitor cell differentiation with an anisotropic pore architecture inspired by the hierarchical collagen structure of AC. The use of this bilayered scaffold resulted in improved tissue repair outcomes in a clinically relevant large animal model, specifically the ability to guide neo-tissue organization and therefore recapitulate key aspects of the zonal structure of native articular cartilage. These bilayer scaffolds have the potential to become a new therapeutic option for osteochondral defect repair, while the biofabrication concept detailed here could be readily translated to other tissues where recapitulation of tissue organization is a key challenge.

Funding

Funding for the project was received from Science Foundation Ireland (12/IA/1554 and 12/RC/2278_P2), Enterprise Ireland (CF/2014/4325) and the European Research Council (ANCHOR – 779909, StemRepair -258463 and JointPrinting – 647004). DCB has also received funding from the Orthoregeneration Network (ON) foundation and the Orthopaedic Research Society (ORS) through a Kick-Starter award. PJDP was funded by the Irish Research Council (GOIPG/2015/3186). FEF received funding from the European Union's Horizon 2020 research and innovation programme under the Marie Skłodowska-Curie Grant Agreement No. 839150.This research was co-funded by the European Regional Development Fund (ERDF) under Ireland's European Structural and Investment Funds Programmes 2014-2020.

Declaration of Competing Interest

The authors declare the following financial interests/personal relationships which may be considered as potential competing interests. Research undertaken in Daniel Kelly's laboratory at Trinity College Dublin is part-funded by Johnson & Johnson services (J&J). J&J did not sponsor or provide any input or direction for this study. The AC-ECM scaffold fabrication procedure detailed in this study is protected by the following patents: EP3180043B1/US20200188556A1 [39].

Acknowledgments

The authors wish to thank the surgical and anesthesia staff and students from the School of Veterinary Medicine, University College Dublin for their assistance with the goat study. Microscopy characterization and analysis was performed at the CRANN Advanced Microscopy Laboratory (AML www.tcd.ie/crann/aml/). Schematic diagrams were created with Biorender.com.

Supplementary materials

Supplementary material associated with this article can be found, in the online version, at doi:10.1016/j.actbio.2022.03.009.

References

[1] M. MacConaill, The movements of bones and joints, J. Bone Joint Surg. 33 (2) (1951) 251–257 British volume.
[2] A. Benninghoff, Form und bau der gelenknorpel in ihren bezeihungen zur funktion, Z. Zellforsch. Mikrosk. Anat. 2 (1925) 783–825.
[3] J.M. Mansour, Biomechanics of cartilage, Kinesiol. Mech. Pathomech. Hum. Mov. 2 (2003) 69–83.
[4] J.M. Clark, The organisation of collagen fibrils in the superficial zones of articular cartilage, J. Anat. 171 (1990) 117–130.
[5] R.J. Lories, F.P. Luyten, The bone-cartilage unit in osteoarthritis, Nat. Rev. Rheumatol. 7 (1) (2011) 43–49.
[6] H.J. Mankin, The reaction of articular cartilage to injury and osteoarthritis (second of two parts), N. Engl. J. Med. 291 (25) (1974) 1335–1340.
[7] P. Behrens, T. Bitter, B. Kurz, M. Russlies, Matrix-associated autologous chondrocyte transplantation/implantation (MACT/MACI)–5-year follow-up, Knee 13 (3) (2006) 194–202.
[8] W. Bartlett, J.A. Skinner, C.R. Gooding, R.W. Carrington, A.M. Flanagan, T.W. Briggs, G. Bentley, Autologous chondrocyte implantation versus matrix-induced autologous chondrocyte implantation for osteochondral defects of the knee: a prospective, randomised study, J. Bone. Joint Surg. Br. 87 (5) (2005) 640–645.
[9] P. Cherubino, F. Grassi, P. Bulgheroni, M. Ronga, Autologous chondrocyte implantation using a bilayer collagen membrane: a preliminary report, J. Orthop. Surg. 11 (1) (2003) 10–15.
[10] B.J. Huang, J.C. Hu, K.A. Athanasiou, Cell-based tissue engineering strategies used in the clinical repair of articular cartilage, Biomaterials 98 (2016) 1–22.
[11] A.M. Yousefi, M.E. Hoque, R.G.S.V. Prasad, N. Uth, Current strategies in multiphasic scaffold design for osteochondral tissue engineering: a review, J. Biomed. Mater. Res. Part A 103 (7) (2015) 2460–2481.
[12] M. Brittberg, Clinical articular cartilage repair—an up to date review, Ann. Joint 3 (2018).
[13] F. Familiari, M.E. Cinque, J. Chahla, J.A. Godin, M.L. Olesen, G. Moatshe, R.F. LaPrade, Clinical outcomes and failure rates of osteochondral allograft transplantation in the knee: a systematic review, Am. J. Sports Med. 46 (14) (2018) 3541–3549.
[14] P. Hindle, J.L. Hendry, J.F. Keating, L.C. Biant, Autologous osteochondral mosaicplasty or TruFit™ plugs for cartilage repair, Knee Surg. Sports Traumatol. Arthrosc. 22 (6) (2014) 1235–1240.
[15] E. Kon, M. Delcogliano, G. Filardo, G. Altadonna, M. Marcacci, Novel nano–composite multi-layered biomaterial for the treatment of multifocal degenerative cartilage lesions, Knee Surg. Sports Traumatol. Arthrosc. 17 (11) (2009) 1312–1315.
[16] E. Kon, G. Filardo, J. Shani, N. Altschuler, A. Levy, K. Zaslav, J.E. Eisman, D. Robinson, Osteochondral regeneration with a novel aragonite-hyaluronate biphasic scaffold: up to 12-month follow-up study in a goat model, J. Orthop. Surg. Res. 10 (1) (2015) 81.
[17] A. Yucekul, D. Ozdil, N.H. Kutlu, E. Erdemli, H.M. Aydin, M.N. Doral, Tri-layered composite plug for the repair of osteochondral defects: *in vivo* study in sheep, J. Tissue Eng. 8 (2017) 2041731417697500.
[18] R. D'Ambrosi, F. Valli, P. De Luca, N. Ursino, F.G. Usuelli, MaioRegen osteochondral substitute for the treatment of knee defects: a systematic review of the literature, J. Clin. Med. 8 (6) (2019) 783.
[19] Y. Zhang, Y. He, S. Bharadwaj, N. Hammam, K. Carnagey, R. Myers, A. Atala, M. Van Dyke, Tissue-specific extracellular matrix coatings for the promotion of cell proliferation and maintenance of cell phenotype, Biomaterials 30 (23-24) (2009) 4021–4028.
[20] S.F. Badylak, The extracellular matrix as a biologic scaffold material, Biomaterials 28 (25) (2007) 3587–3593.
[21] B.N. Brown, S.F. Badylak, Extracellular matrix as an inductive scaffold for functional tissue reconstruction, Transl. Res. 163 (4) (2014) 268–285.
[22] G.M. Cunniffe, P.J. Díaz-Payno, E.J. Sheehy, S.E. Critchley, H.V. Almeida, P. Pitacco, S.F. Carroll, O.R. Mahon, A. Dunne, T.J. Levingstone, C.J. Moran, R.T. Brady, F.J. O'Brien, P.A.J. Brama, D.J. Kelly, Tissue-specific extracellular matrix scaffolds for the regeneration of spatially complex musculoskeletal tissues, Biomaterials 188 (2019) 63–73.
[23] D.C. Browe, O.R. Mahon, P.J. Diaz-Payno, N. Cassidy, I. Dudurych, A. Dunne, C.T. Buckley, D.J. Kelly, Glyoxal cross-linking of solubilized extracellular matrix to produce highly porous, elastic, and chondro-permissive scaffolds for orthopedic tissue engineering, J. Biomed. Mater. Res. A 107 (10) (2019) 2222–2234.
[24] O.R. Mahon, D.C. Browe, P.J. Diaz-Payno, P. Pitacco, K.T. Cunningham, K.H.G. Mills, A. Dunne, D.J. Kelly, Extracellular matrix scaffolds derived from different musculoskeletal tissues drive distinct macrophage phenotypes and direct tissue-specific cellular differentiation, J. Immunol. Regener. Med. (2021) 100041.
[25] K.E. Benders, W. Boot, S.M. Cokelaere, P.R. Van Weeren, D. Gawlitta, H.J. Bergman, D.B. Saris, W.J. Dhert, J. Malda, Multipotent stromal cells outperform chondrocytes on cartilage-derived matrix scaffolds, Cartilage 5 (4) (2014) 221–230.
[26] A.J. Sutherland, G.L. Converse, R.A. Hopkins, M.S. Detamore, The bioactivity of cartilage extracellular matrix in articular cartilage regeneration, Adv. Healthc. Mater. 4 (1) (2015) 29–39.
[27] G. Tian, S. Jiang, J. Li, F. Wei, X. Li, Y. Ding, Z. Yang, Z. Sun, K. Zha, F. Wang, Cell-free decellularized cartilage extracellular matrix scaffolds combined with interleukin 4 promote osteochondral repair through immunomodulatory macrophages: *in vitro* and *in vivo* preclinical study, Acta Biomater. (2021).
[28] F.E. Freeman, D.C. Browe, J. Nulty, S. Von Euw, W.L. Grayson, D.J. Kelly, Biofabrication of multiscale bone extracellular matrix scaffolds for bone tissue engineering, Eur. Cell Mater. 38 (2019) 168–187.
[29] B.B. Rothrauff, R.S. Tuan, Decellularized bone extracellular matrix in skeletal tissue engineering, Biochem. Soc. Trans. 48 (3) (2020) 755–764.
[30] B.P. Hung, B.A. Naved, E.L. Nyberg, M. Dias, C.A. Holmes, J.H. Elisseeff, A.H. Dorafshar, W.L. Grayson, Three-dimensional printing of bone extracellular matrix for craniofacial regeneration, ACS Biomater. Sci. Eng. 2 (10) (2016) 1806–1816.
[31] G.M. Cunniffe, P.J. Diaz-Payno, J.S. Ramey, O.R. Mahon, A. Dunne, E.M. Thompson, F.J. O'Brien, D.J. Kelly, Growth plate extracellular matrix-derived scaffolds for large bone defect healing, Eur. Cell Mater. 33 (2017) 130–142.
[32] L. Luo, R. Eswaramoorthy, K.J. Mulhall, D.J. Kelly, Decellularization of porcine articular cartilage explants and their subsequent repopulation with human chondroprogenitor cells, J. Mech. Behav. Biomed. Mater. 55 (2015) 21–31.
[33] E.L. de Mulder, G. Hannink, T.H. van Kuppevelt, W.F. Daamen, P. Buma, Similar hyaline-like cartilage repair of osteochondral defects in rabbits using isotropic and anisotropic collagen scaffolds, Tissue Eng. Part A 20 (3-4) (2014) 635–645.
[34] H. Joukhdar, A. Seifert, T. Jüngst, J. Groll, M.S. Lord, J. Rnjak-Kovacina, Ice templating soft matter: fundamental principles and fabrication approaches to tailor pore structure and morphology and their biomedical applications, Adv. Mater. (2021) 2100091.
[35] K.F. Eichholz, D.A. Hoey, Mediating human stem cell behaviour via defined fibrous architectures by melt electrospinning writing, Acta Biomater. 75 (2018) 140–151.
[36] T. Zhang, H. Zhang, L. Zhang, S. Jia, J. Liu, Z. Xiong, W. Sun, Biomimetic design and fabrication of multilayered osteochondral scaffolds by low-temperature deposition manufacturing and thermal-induced phase-separation techniques, Biofabrication 9 (2) (2017) 025021.
[37] S.R. Caliari, B.A. Harley, The effect of anisotropic collagen-GAG scaffolds and growth factor supplementation on tendon cell recruitment, alignment, and metabolic activity, Biomaterials 32 (23) (2011) 5330–5340.

[38] V. Kroehne, I. Heschel, F. Schügner, D. Lasrich, J. Bartsch, H. Jockusch, Use of a novel collagen matrix with oriented pore structure for muscle cell differentiation in cell culture and in grafts, J. Cell. Mol. Med. 12 (5a) (2008) 1640–1648.
[39] S. Jia, L. Liu, W. Pan, G. Meng, C. Duan, L. Zhang, Z. Xiong, J. Liu, Oriented cartilage extracellular matrix-derived scaffold for cartilage tissue engineering, J. Biosci. Bioeng. 113 (5) (2012) 647–653.
[40] C.M. Murphy, M.G. Haugh, F.J. O'Brien, The effect of mean pore size on cell attachment, proliferation and migration in collagen-glycosaminoglycan scaffolds for bone tissue engineering, Biomaterials 31 (3) (2010) 461–466.
[41] M.G. Haugh, C.M. Murphy, F.J. O'Brien, Novel freeze-drying methods to produce a range of collagen–glycosaminoglycan scaffolds with tailored mean pore sizes, Tissue Eng. Part C Methods 16 (5) (2010) 887–894.
[42] N. Reznikov, R. Almany-Magal, R. Shahar, S. Weiner, Three-dimensional imaging of collagen fibril organization in rat circumferential lamellar bone using a dual beam electron microscope reveals ordered and disordered sub-lamellar structures, Bone 52 (2) (2013) 676–683.
[43] H.V. Almeida, Y. Liu, G.M. Cunniffe, K.J. Mulhall, A. Matsiko, C.T. Buckley, F.J. O'Brien, D.J. Kelly, Controlled release of transforming growth factor-beta3 from cartilage-extra-cellular-matrix-derived scaffolds to promote chondrogenesis of human-joint-tissue-derived stem cells, Acta Biomater. 10 (10) (2014) 4400–4409.
[44] N.Y. Ignat'eva, N.A. Danilov, S.V. Averkiev, M.V. Obrezkova, V.V. Lunin, E.N. Sobol, Determination of hydroxyproline in tissues and the evaluation of the collagen content of the tissues, J. Anal. Chem. 62 (1) (2007) 51–57.
[45] J. Nulty, F.E. Freeman, D.C. Browe, R. Burdis, D.P. Ahern, P. Pitacco, Y.B. Lee, E. Alsberg, D.J. Kelly, 3D bioprinting of prevascularised implants for the repair of critically-sized bone defects, Acta Biomater. (2021).
[46] T.J. Levingstone, A. Ramesh, R.T. Brady, P.A.J. Brama, C. Kearney, J.P. Gleeson, F.J. O'Brien, Cell-free multi-layered collagen-based scaffolds demonstrate layer specific regeneration of functional osteochondral tissue in caprine joints, Biomaterials 87 (2016) 69–81.
[47] A.M. Getgood, S.J. Kew, R. Brooks, H. Aberman, T. Simon, A.K. Lynn, N. Rushton, Evaluation of early-stage osteochondral defect repair using a biphasic scaffold based on a collagen–glycosaminoglycan biopolymer in a caprine model, Knee 19 (4) (2012) 422–430.
[48] P. Mainil-Varlet, B. Van Damme, D. Nesic, G. Knutsen, R. Kandel, S. Roberts, A new histology scoring system for the assessment of the quality of human cartilage repair: ICRS II, Am. J. Sports Med. 38 (5) (2010) 880–890.
[49] F. Varghese, A.B. Bukhari, R. Malhotra, A. De, IHC Profiler: an open source plugin for the quantitative evaluation and automated scoring of immunohistochemistry images of human tissue samples, PLoS One 9 (5) (2014) e96801.
[50] B. Andrée, A. Bär, A. Haverich, A. Hilfiker, Small intestinal submucosa segments as matrix for tissue engineering, Tissue Eng. Part B Rev. 19 (4) (2013) 279–291.
[51] A. Shridhar, B.G. Amsden, E.R. Gillies, L.E. Flynn, Investigating the effects of tissue-specific extracellular matrix on the adipogenic and osteogenic differentiation of human adipose-derived stromal cells within composite hydrogel scaffolds, Front. Bioeng. Biotechnol. (2019) 402.
[52] B.B. Rothrauff, G. Yang, R.S. Tuan, Tissue-specific bioactivity of soluble tendon-derived and cartilage-derived extracellular matrices on adult mesenchymal stem cells, Stem Cell Res. Ther. 8 (1) (2017) 133.
[53] G.M. Cunniffe, P.J. Diaz-Payno, E.J. Sheehy, S.E. Critchley, H.V. Almeida, P. Pitacco, S.F. Carroll, O.R. Mahon, A. Dunne, T.J. Levingstone, C.J. Moran, R.T. Brady, F.J. O'Brien, P.A.J. Brama, D.J. Kelly, Tissue-specific extracellular matrix scaffolds for the regeneration of spatially complex musculoskeletal tissues, Biomaterials 188 (2019) 63–73.
[54] A. Matsiko, J.P. Gleeson, F.J. O'Brien, Scaffold mean pore size influences mesenchymal stem cell chondrogenic differentiation and matrix deposition, Tissue Eng. Part A 21 (3-4) (2015) 486–497.
[55] Q. Zhang, H. Lu, N. Kawazoe, G. Chen, Pore size effect of collagen scaffolds on cartilage regeneration, Acta Biomater. 10 (5) (2014) 2005–2013.
[56] M.M. Nava, L. Draghi, C. Giordano, R. Pietrabissa, The effect of scaffold pore size in cartilage tissue engineering, J. Appl. Biomater. Funct. Mater. 14 (3) (2016) e223–e229.
[57] P. Duan, Z. Pan, L. Cao, Y. He, H. Wang, Z. Qu, J. Dong, J. Ding, The effects of pore size in bilayered poly(lactide-co-glycolide) scaffolds on restoring osteochondral defects in rabbits, J. Biomed. Mater. Res. Part A 102 (1) (2014) 180–192.
[58] Y. Sun, L. Yan, S. Chen, M. Pei, Functionality of decellularized matrix in cartilage regeneration: a comparison of tissue versus cell sources, Acta Biomater. 74 (2018) 56–73.
[59] D. Gawlitta, K.E. Benders, J. Visser, A.S. van der Sar, D.H. Kempen, L.F. Theyse, J. Malda, W.J. Dhert, Decellularized cartilage-derived matrix as substrate for endochondral bone regeneration, Tissue Eng. Part A 21 (3-4) (2015) 694–703.
[60] H. Xie, Z. Wang, L. Zhang, Q. Lei, A. Zhao, H. Wang, Q. Li, Y. Cao, W.J. Zhang, Z. Chen, Extracellular vesicle-functionalized decalcified bone matrix scaffolds with enhanced pro-angiogenic and pro-bone regeneration activities, Sci. Rep. 7 (1) (2017) 1–13.
[61] M. Tamaddon, M. Burrows, S.A. Ferreira, F. Dazzi, J.F. Apperley, A. Bradshaw, D.D. Brand, J. Czernuszka, E. Gentleman, Monomeric, porous type II collagen scaffolds promote chondrogenic differentiation of human bone marrow mesenchymal stem cells *in vitro*, Sci. Rep. 7 (2017) 43519.
[62] A. International, Standard Guide for *In Vivo* Assessment of Implantable Devices Intended to Repair or Regenerate Articular Cartilage, ASTM International Conshohocken, PA, 2005.
[63] S. Patil, N. Steklov, L. Song, W.C. Bae, D.D. D'Lima, Comparative biomechanical analysis of human and caprine knee articular cartilage, Knee 21 (1) (2014) 119–125.
[64] C.J. Moran, A. Ramesh, P.A. Brama, J.M. O'Byrne, F.J. O'Brien, T.J. Levingstone, The benefits and limitations of animal models for translational research in cartilage repair, J. Exp. Orthop. 3 (1) (2016) 1–12.
[65] J. Cook, C. Hung, K. Kuroki, A. Stoker, C. Cook, F. Pfeiffer, S. Sherman, J. Stannard, Animal models of cartilage repair, Bone Joint Res. 3 (4) (2014) 89–94.
[66] U. Food, D. Administration, Guidance for Industry: Preparation of IDEs and INDs for Products Intended to Repair or Replace Knee Cartilage, US Food and Drug Administration, Washington, DC, 2011.
[67] D.W. Levine, L. Mondano, M. Halpin, FDA regulatory pathways for knee cartilage repair products, Sports Med. Arthrosc. Rev. 16 (4) (2008) 202–207.
[68] G.D. Jay, K.A. Waller, The biology of lubricin: near frictionless joint motion, Matrix Biol. 39 (2014) 17–24.
[69] Y. Lee, J. Choi, N.S. Hwang, Regulation of lubricin for functional cartilage tissue regeneration: a review, Biomater Res. 22 (1) (2018) 9.
[70] X.L. Lu, V.C. Mow, Biomechanics of articular cartilage and determination of material properties, Med. Sci. Sports Exerc. 40 (2) (2008) 193–199.
[71] Q. Meng, S. An, R.A. Damion, Z. Jin, R. Wilcox, J. Fisher, A. Jones, The effect of collagen fibril orientation on the biphasic mechanics of articular cartilage, J. Mech. Behav. Biomed. Mater. 65 (2017) 439–453.
[72] A.J. Sophia Fox, A. Bedi, S.A. Rodeo, The basic science of articular cartilage: structure, composition, and function, Sports Health 1 (6) (2009) 461–468.
[73] M.B. Hurtig, M.D. Buschmann, L.A. Fortier, C.D. Hoemann, E.B. Hunziker, J.S. Jurvelin, P. Mainil-Varlet, C.W. McIlwraith, R.L. Sah, R.A. Whiteside, Preclinical studies for cartilage repair: recommendations from the international cartilage repair society, Cartilage 2 (2) (2011) 137–152.
[74] O.R. Mahon, D.C. Browe, T. Gonzalez-Fernandez, P. Pitacco, I.T. Whelan, S. Von Euw, C. Hobbs, V. Nicolosi, K.T. Cunningham, K.H. Mills, Nano-particle mediated M2 macrophage polarization enhances bone formation and MSC osteogenesis in an IL-10 dependent manner, Biomaterials 239 (2020) 119833.
[75] B. Wang, P.J. Díaz-Payno, D.C. Browe, F.E. Freeman, J. Nulty, R. Burdis, D.J. Kelly, Affinity-bound growth factor within sulfated interpenetrating network bioinks for bioprinting cartilaginous tissues, Acta Biomater. 128 (2021) 130–142.
[76] F.E. Freeman, P. Pitacco, L.H. van Dommelen, J. Nulty, D.C. Browe, J.Y. Shin, E. Alsberg, D.J. Kelly, 3D bioprinting spatiotemporally defined patterns of growth factors to tightly control tissue regeneration, Sci. Adv. 6 (33) (2020) eabb5093.